Temporal dynamics of the deep-sea pink urchin *Strongylocentrotus fragilis* on the Northeast Pacific continental margin

Rylan J. Command, Fabio C. De Leo, & Katleen Robert

2023

Deep–Sea Research I 193 (2023) 103958

Contents lists available at ScienceDirect

Deep-Sea Research Part I

journal homepage: www.elsevier.com/locate/dsri

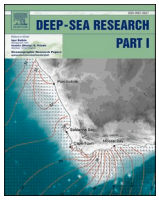

Temporal dynamics of the deep-sea pink urchin *Strongylocentrotus fragilis* on the Northeast Pacific continental margin

Rylan J. Command [a,*], Fabio C. De Leo [b,c], Katleen Robert [a]

[a] Fisheries and Marine Institute, Memorial University of Newfoundland, St. John's, Newfoundland and Labrador, Canada
[b] Ocean Networks Canada, University of Victoria, Victoria, British Columbia, Canada
[c] Department of Biology, University of Victoria, Victoria, British Columbia, Canada

ARTICLE INFO

Keywords:
Marine heatwaves
Continental margin
Cabled-observatories
Deep sea
Time series

ABSTRACT

The Northeast Pacific continental margin is characterized by strong seasonal upwelling, which drives high primary productivity, and supports high diversity and biomass of benthic megafauna. The recent occurrence of a marine heat wave ("The Blob", *sensu* Kintisch, 2015) in 2013–2016 resulted in changes to phytoplankton community composition and loss of coastal kelp abundance and diversity, reducing gross primary productivity in the region. However, cumulative effects of marine heat waves and ongoing basin-scale deoxygenation in deep-sea ecosystems remain poorly understood. Here, we use a 7-year time series of physicochemical and video imagery data from Ocean Networks Canada's NEPTUNE observatory to investigate temporal dynamics of the deep-sea pink urchin *Strongylocentrotus fragilis* in relation to multi-year environmental variability. Using generalized additive models, we show that local *S. fragilis* density at Barkley Upper Slope (420 m) fluctuated over time and was partially explained by changes in dissolved oxygen concentration and suspended particulate matter in the benthic boundary layer (ADCP backscatter), with high urchin density corresponding to high oxygen and low backscatter. Seafloor dissolved oxygen ranged from 0.80 to 1.89 mL/L and varied seasonally, exhibiting a clear negative correlation with sea surface primary productivity (MODIS satellite Chl-a data), corresponding with the onset of yearly upwelling conditions. However, during the anomalously warm years affected by 'The Blob', dampened upwelling maintained higher dissolved oxygen conditions near the seafloor. *S. fragilis* density declined during 'Blob' conditions, likely in response to reduced kelp and phytodetritus subsidies from coastal waters. We propose a foraging-respiration trade-off hypothesis, whereby *S. fragilis* forages in deeper water during weak upwelling and migrates to shallower habitats during low oxygen conditions. *S. fragilis* is an important bioturbator and detritivore; changes in the density and distribution of this species may directly affect sediment turnover rates and nutrient cycling on the continental margin, with consequences for surface and coastal productivity.
https://github.com/rjcommand/.

1. Introduction

The continental margin of the Northeast Pacific Ocean (NEP) is characterized as an Eastern Boundary Current Ecosystem, where strong upwelling brings cool, nutrient-rich water from the deep-sea up to the surface (Rossi et al., 2009; Chavez and Messié 2009). Seasonal upwelling maintains high primary productivity in offshore surface waters (Arntz et al., 2006) and dense kelp forests along the coast (Edwards 2004), fueling productive fisheries (Ware and Thomson 1991). Phytodetritus eventually sinks to the seafloor, providing a large source of organic carbon and nutrients to deep-sea communities (Billett et al., 1983; Lampitt 1985; Gage and Tyler 1991; Smith et al., 1993, 1994; Ruhl and Smith Jr., 2004). This organic matter is the primary food source for many benthic megafauna species (Smith et al., 1994; Billett et al., 2010; Glover et al., 2010; Birchenough et al., 2015; Campanyà-Llovet et al., 2018; Durden et al., 2020), that make up much of the biomass (Levin et al., 2015; Fredriksen et al., 2020) and drive biogeochemical cycling (Turner 2015; Thomsen et al., 2017) in the deep sea. Where respiration of sinking phytodetritus outweighs natural reoxygenation processes, a region of permanently low dissolved oxygen (<0.5 mL/L) can form, known as an Oxygen Minimum Zone (OMZ, Helly and Levin, 2004). Benthic megafaunal species densities and richness is highest on the OMZ

* Corresponding author.
E-mail address: rylan.command@mi.mun.ca (R.J. Command).

https://doi.org/10.1016/j.dsr.2022.103958
Received 3 February 2022; Received in revised form 30 September 2022; Accepted 21 December 2022
Available online 24 December 2022

margins, decreasing towards the OMZ core where dissolved oxygen is lowest (Levin 2003). The distribution of oxygen on the continental margin also influences the spatiotemporal distribution of benthic communities (Levin 2003; Helly and Levin 2004; Papiol et al., 2017), with direct consequences for nutrient cycling and benthopelagic coupling (Lebrato et al., 2010; Levin and Sibuet 2012; Kendzierska et al., 2020).

Organic matter export to the seafloor varies on seasonal, interannual, and decadal scales (Billett et al., 1983; Bett et al., 2001; Smith et al., 2018), and the amount of food available to the benthos is directly related to surface productivity (Honjo et al., 2014; Thomsen et al., 2017). Marine heatwaves (MHW) – extended periods of anomalously warm water (Sorte et al., 2010) – cause thermal stratification in the upper ocean, inhibiting upwelling and nutrient flux that drives primary productivity (Kintisch 2015), and reducing the downward flux of organic matter between the surface and benthos along the continental margin. In the NEP, a MHW dubbed "The Blob" was observed off the coast of British Columbia and the western United States at the end of 2013 and persisted until early 2016 (Cavole et al., 2016), with long-lasting ecological and oceanographic effects in some areas (Jackson et al., 2018a; McPherson et al., 2021; Suryan et al., 2021). The Blob resulted in the loss of kelp abundance and diversity (Starko et al., 2019), changes to phytoplankton community composition (Cavole et al., 2016), and reduced gross primary productivity (Yang et al., 2018), with likely consequences for benthic megafauna that rely on phytodetritus for food (Brodeur et al., 2019). MHWs are becoming more common and lasting longer (Scannell et al., 2016; Oliver et al., 2018), causing harmful algal blooms (McCabe et al., 2016; McKibben et al., 2017; Trainer et al., 2020), reduced fish recruitment (Cavole et al., 2016), and fisheries closures (Ritzman et al., 2018). Most of the research on the 2013–2016 MHW has focused on the pelagic and nearshore realms (Cavole et al., 2016; Auth et al., 2018; Batten et al., 2018) and abyssal plain (Smith et al., 2018; Kuhnz et al., 2020), however the extent to which benthic megafauna on the continental margin were affected by these events remains understudied. Many organisms are well adapted to their thermal niche (Bates et al., 2010) and will rapidly recover once conditions return to normal (Heise 2006; Gleason and Burton 2013; Kelly et al., 2017). However, the persistence and increasing prevalence of warm water anomalies is causing potentially permanent damage to marine ecosystems (Couch et al., 2017; Jackson et al., 2018b; Suryan et al., 2021).

The distribution and availability of food and oxygen on the NEP continental margin is further influenced locally by topographic features such as submarine canyons, which steer Ekman-driven current flows enhancing coastal upwelling (Allen and de Madron 2009; Ramos-Musalem and Allen 2019). Submarine canyons also play a key role in structuring slope and deep-sea ecosystems since they affect the distribution of food on the seafloor by trapping and funneling zooplankton, detrital and sedimentary organic matter from shallower shelf areas into the slope (Vetter and Dayton 1999; Puig et al., 2014; De Leo et al., 2018). Perhaps the best studied submarine canyon on British Columbia's coast is Barkley Canyon, in particular after the installation of the NEPTUNE cabled observatory in 2009 (Best et al., 2007). The local current regime affected by the canyon's topography has been extensively studied prior to NEPTUNE, and is known to enhance local upwelling and primary productivity in surface waters above the canyon (Mackas et al., 1997; Allen et al., 2001; Genin 2004). Secondary production resulting from zooplankton aggregations and decomposing organic matter is also transported down into Barkley Canyon's deeper waters (Baker and Hickey 1986; Allen and de Madron 2009; De Leo et al., 2018). The canyon cuts across the slope impinging the core of the OMZ at about 900 m, where dissolved oxygen can reach as low as 0.16 mL/L (Domke et al., 2017). In contrast, the adjacent upper slope (400 m) experiences higher, though more variable, oxygen concentrations, ranging from 0.79 mL/L to 1.94 mL/L, making this an ideal site to study megafaunal responses to short- and long-term variable ocean conditions. Extensive research on the temporal dynamics of megafauna within Barkley Canyon has been conducted (Juniper et al., 2013; Doya et al., 2014; Matabos et al., 2014; Chatzievangelou et al., 2016, 2020; Domke et al., 2017; Chauvet et al., 2018) and interannual ontogenetic migration of tanner crab, *Chionoecetes tanneri* (Chauvet et al., 2019), however, considerably less attention has been given to the adjacent slope ecosystem (Robert and Juniper 2012; De Leo et al., 2017; Chauvet et al., 2018).

One of the dominant megafauna at the upper slope near Barkley Canyon is the deep-sea pink urchin *Strongylocentrotus fragilis* Jackson, 1912 (Robert and Juniper 2012; De Leo et al., 2017). *S. fragilis* is a detritivore that forages on a wide range of detritus, though many studies point to a diet predominantly composed of large macroalgal detritus and other phytodetritus arriving at the seafloor from the surface and coastal waters (Booloottian et al., 1959; Filbee-Dexter and Scheibling 2014; Campanyà-Llovet et al., 2018). *S. fragilis* plays an important role in deep-sea nutrient cycling through locomotion and grazing, which contributes to sediment turnover (Robert and Juniper 2012) and enhances nutrient availability in the water column (Thompson and Riddle 2005). *S. fragilis* forms large feeding aggregations on the continental margin (De Leo et al., 2017), influencing the composition and spatial distribution of nutrients and sediment infaunal communities (Campanyà-Llovet et al., 2018). As slow-moving, calcifying organisms, sea urchins are particularly susceptible to climate change (Delorme and Sewell 2014; Asnaghi et al., 2020; Low and Micheli 2020). Previous research has found that calcification rates and reproductive capacity of *S. fragilis* are affected by food availability, ocean warming, acidification, and deoxygenation, with reduced recruitment and survival already occurring under current ocean conditions (Sato et al., 2018).

In this paper, we used long-term (7-year) and high-frequency video and environmental time-series data from the NEPTUNE observatory at the Barkley Canyon Upper Slope (BCUS) location to study how *S. fragilis* densities respond to seasonal and inter-annual variability in oceanographic conditions. In particular, we draw focus to the 2013–2016 marine heatwave that affected more than 2.5 million km^2 of the NEP (Bond et al., 2015). "The Blob" reportedly caused reduction in coastal upwelling, with consequent decrease in primary and secondary productivity, with a range of effects in restructuring local and regional food-webs (Cavole et al., 2016; Brodeur et al., 2019). Since *S. fragilis* plays a key role in benthic-pelagic coupling and nutrient recycling over the shelf and slope, it is crucial to understand how this species is affected by large-scale, climate-driven ecosystem changes.

We contrasted the high frequency time-series observations from NEPTUNE against a 14-year, bi-annual bottom trawl survey conducted on the West Coast of Vancouver Island by Fisheries and Oceans Canada (DFO). The trawl survey database was used to extract *S. fragilis* densities and distribution across a broader spatial scale and along a depth gradient to be used as a possible predictor of local population fluctuations quantified from video imagery at the single fixed location of the seafloor observatory. In addition, we also used climatology data of sea-surface temperature (SST) and colour irradiance (as a proxy for chlorophyll-*a*) from an offshore meteorological buoy and from the MODIS Aqua OceanColour satellite, respectively to understand the broader oceanographic effects of "The Blob" in the region. We hypothesized that 1) *S. fragilis* density on the continental margin declined during "The Blob" due to reduced upwelling food supply disruption, and 2) *S. fragilis* depth distribution shoaled over time due to the expanding OMZ.

2. Methods

2.1. Study site

The study area was located on the continental slope off Vancouver Island adjacent to the northern flank of Barkley Canyon (Fig. 1A). This canyon incises the continental shelf from 200 m at its head (Allen et al., 2001) and reaches 2660 m the Cascadia Basin at, providing a link between the continental margin and an abyssal plain. The details of the flow regime around Barkley Canyon have been described by Allen et al. (2001). In brief, seasonal upwelling-favourable winds in summer result

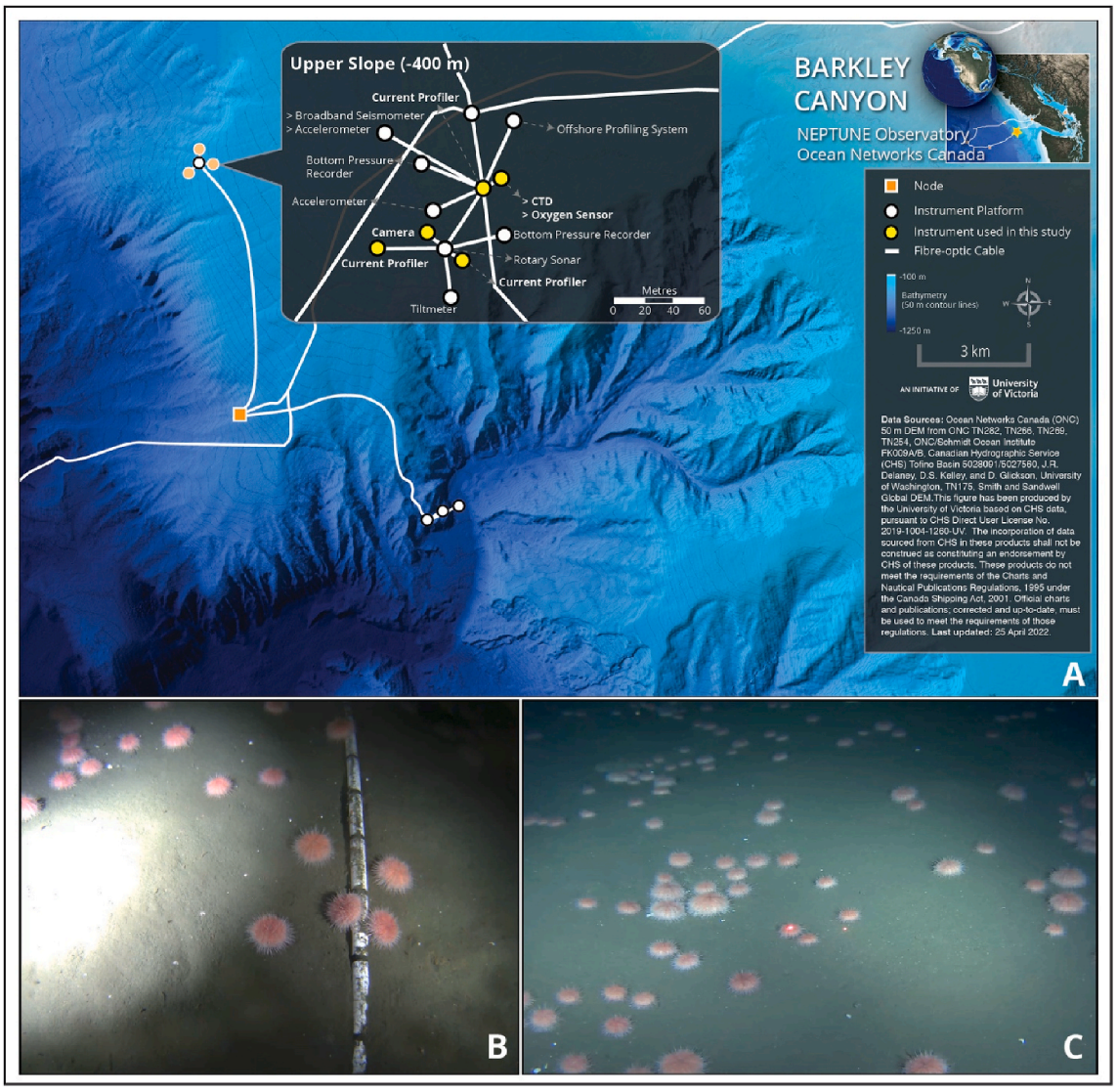

Fig. 1. Map of the study area showing the NEPTUNE cabled observatory infrastructure at Barkley Canyon and Upper Slope (A). Examples of two seafloor camera fields of views for November 2013 (B), and January 2020 (C).

in stronger up-canyon flow, moving deep, low oxygen water from the OMZ onto the slope, and cold, nutrient rich water from the sub-pycnocline closer to the surface, enhancing primary productivity (Allen et al., 2001). In winter when downwelling winds are dominant, deep wind-driven mixing forces oxygen-rich surface water down onto the slope. Short-lived phytoplankton blooms also occur during winter/-downwelling conditions, and rapidly export particulate carbon through the main canyon axis (Thomsen et al., 2017). Aside from the seasonal fluctuations of the upper boundary, the dissolved oxygen levels and the main depth boundaries of the OMZ are relatively stable.

This study was conducted at the Barkley Canyon Upper Slope site (BCUS), on the slope about 3 km from the canyon and connected to the network at 396 m depth (Fig. 1A; 48° 25′ 37.2″N, 126° 10′ 29.7″W). The seafloor at the BCUS site is characterized by soft sediments and a high abundance of *S. fragilis*, solariellidae snails, and rockfish (*Sebastes* spp., Chauvet 2018).

2.2. Estimating S. fragilis densities from imagery

We analyzed footage from a video camera mounted on the BCUS platform from 2013 to 2020 (Fig. 1B and C). Four different high-definition video camera systems have been used during the entire 7-year study period (Table 1). The footage quality progressively improved as each new camera system deployed followed NEPTUNE observatory's continuous progress towards better configuration of seafloor instrument platforms, digital infrastructure, software controls, and data archiving. In all systems, the camera was mounted on a galvanized steel tripod and attached to a Remote Ocean Systems (ROS) pan and tilt system, allowing for 360° of pan angle rotation and thus covering the seafloor in all directions (Chauvet 2018; De Leo et al., 2018). Between years, the camera tripod configurations changed slightly, with the final height of the camera lenses above the seabed varying between 40 and 95 cm, thus altering the total imaged area of the seafloor (Table 1). Two ROS LED lights (100 W, >406 lm, De Leo et al., 2018) provided illumination during video recordings. The cameras followed the same recording schedule since June 15, 2012 (i.e. recording 5 min videos every 2 h, changing to an hourly recording interval on September 19, 2019). This recording schedule was designed to minimize the impact of artificial lighting on the behaviour of benthic organisms (Widder et al., 2005) and was optimized for detecting sea urchin abundance patterns (Robert and Juniper 2012). We analyzed 4 video sequences each day (0000–0005, 0600–0605, 1200–1205, and 1800–1805 UTC) in order to account for diurnal and tidal variation (Aguzzi and Company 2010). In each video, the number of *S. fragilis* present were counted and densities

Table 1
Video camera deployments for each time-series sampling period at the Barkley Canyon Upper Slope.

Date	Camera System, pixel resolution, frame rate	Camera mounting height (cm)	Field of view angles (horizontal, vertical °)	Pan and tilt angles	Total seafloor area imaged (m^2)
2013-08-15 to 2014-02-03	SubC Imaging Dragonfish 1080p, 30 fps	45	54.7, 34.4	Fixed 45° tilt	0.5
2014-08-15 to 2015-01-12	SubC Imaging Dragonfish 1080p, 30 fps	45	54.7, 34.4	Fixed 63° tilt, 215.24° Pan	14.4
2018-08-15 to 2018-11-23	SubC Imaging Dragonfish 1080p, 30 fps	95	54.7, 34.4	76° tilt sweep	9.33
2019-09-14 to 2020-02-03	Axis Sony P134 SubAqua, 1080p, 23 fps	85	54.7, 34.4	76° tilt sweep, 180° pan sweep	14.93

obtained by dividing the total count of individuals by the total area of imaged seafloor, which varied among the four camera deployments, and expressed in urchins per meters squared (see Table 1). *S. fragilis* were manually counted using ONC's SeaTube web-based video playback interface (https://data.oceannetworks.ca/SeaTube). All video imagery data used in the present study are freely accessible for playback and download at https://data.oceannetworks.ca/DataSearch.

Very unfortunately, two fishing trawling incidents damaged some of the observatory seafloor infrastructure, including the node supplying power to the instruments on one occasion, and another directly hitting the BCUS platform with the seafloor video camera. These events resulted in relatively long stretches of missing data. Due to the trawling incidents, and for the purpose of a meaningful multi-year comparative analysis, we split the dataset into 4 segments (2013–2014, 2014–2015, 2018, and 2019–2020), corresponding to a total of 565 days. Video data time series from each year covered at least partially late summer, fall and winter conditions (Table 1).

S. fragilis has a patchy distribution on the continental slope (Robert and Juniper 2012; Campanyà-Llovet et al., 2018), which could influence abundance and density estimates obtained using imagery from fixed-position observatories. Thus, we used the full field of view available in each sampling interval to cover as much of the seafloor around the observatory as possible. Field of views were calculated following the trigonometric approach of Wakefield and Genin (1987) and Nakajima et al. (2014) using the known height of each camera above the seabed, and the horizontal and vertical acceptance angles of each camera (Table 1). The procedure for calculating the area covered by each camera is outlined in the supplemental material (Appendix 1).

2.3. Environmental data from the seafloor and sea-surface

Environmental data were obtained from instrument sensors on the BCUS platform (Fig. 1B) as well as from a nearby meteorological buoy and the MODIS satellite (Table 2). Dissolved oxygen concentration (mL/L) was collected from a Sea-Bird SBE 63 Dissolved Oxygen Sensor. Salinity (psu) was collected from a Conductivity-Temperature-Depth (CTD) sensor (Sea-Bird SBE 16 plus V2 SEACAT C-T Recorder). These data were collected at a rate of 1 measurement/second.

Benthic boundary layer currents (BBLc) were measured in m/s as *u* (east-west) and *v* (north-south) vectors from an upward-looking Nortek Aquadop 2 MHz Acoustic Doppler Current-Profiler (ADCP). The ADCP collected data in 1.43 cm range bins from the sonar transducer head, approximately 20 cm above the seabed, up to 1.5 m above the seabed, and we averaged current velocities across the full range for each time point (Grant Garner, pers comm.). We then calculated the current direction (°True) and magnitude of the resulting current velocity vector from the *u* and *v* velocity components. Temperature (°C) and pressure (dbar) were also obtained from the ADCP since its time-series had fewer missing values during the study period than the CTD. We also collected the backscatter (Hz) from the ADCP as a proxy for particulate matter in the water column immediately above the seafloor. The ADCP data were collected at a rate of 1 measurement/10 s.

Table 2
List of instruments, sampling frequencies, measured environmental variables, and their units for data collected at the upper slope of Barkley Canyon (48° 25′ 37.2″N, 126° 10′ 29.7″W), weather data collected from the La Perouse Bank buoy (48° 49′ 48″N, 126° 0′ 0″W), Tofino, British Columbia and MODIS satellite. Data were collected from August 15, 2013 to February 3, 2014, August 15, 2014 to January 15, 2015, August 15, 2018 to November 24, 2018, and September 11, 2019 to February 3, 2020.

Sampling Site	Instruments	Measured variables	Sampling frequency	Units
Seafloor data	2 MHz ADCP	v (Northward BBLc)	10 s	m/s
		u (Eastward BBLc)	10 s	m/s
		Temperature	10 s	°C
		Pressure	10 s	dbar
		Backscatter	10 s	Hz
	CTD			
		Salinity	1 s	psu
	Oxygen optode	Oxygen	10 s	mL/L
Weather data	La Perouse Bank Meteorological buoy	SST	2 h	°C
(all years except 2018)	NASA Satellites	Chlorophyll-a	8 days	mg/m^3
Sea surface data				

We used 8-day averaged satellite chlorophyll-a concentration data from MODIS, NASA Earth Observations Goddard Ocean Colour Group (https://oceancolor.gsfc.nasa.gov/l3/order/) for an area around BCUS (Fig. S1) to quantify temporal variability in sea surface primary productivity. The 8-day average allowed for more reliable coverage and helped account for the effects of cloud cover. The chlorophyll-a time-series was derived by averaging the chlorophyll-a concentration over the entire area for which points were extracted (Fig. S1; Chauvet et al., 2018).

Following Chauvet et al. (2018), we acquired SST from the Fisheries and Oceans Canada (DFO) La Perouse Bank Buoy 46,206 (48° 49′ 48″N, 126° 0′ 0″W, http://www.meds-sdmm.dfo-mpo.gc.ca/). To match the temporal resolution of the chlorophyll-*a* time series, we averaged the SST data into 8-day bins. Then to assess the effect of SST anomalies, such as the 2013–2016 Warm Blob event (Bond et al., 2015; Cavole et al., 2016), we calculated anomalous SST (SSTa) as the difference between each 8-day-binned SST measurement and the average SST from the entire buoy time series (1985–2020).

All environmental time series (except SSTa and chlorophyll-*a*) were averaged in 6-h bins corresponding to the sampling period and frequency of the video time-series.

2.4. Bottom trawl surveys (2004–2018)

Every other year since 2004, DFO in collaboration with the Canadian

Groundfish Research and Conservation Society has conducted fisheries-independent synoptic bottom trawl surveys on the continental shelf and slope on the West Coast of Vancouver Island (Anderson et al., 2019). These surveys followed a random depth-stratified sampling design with sampling conducted in 2 km × 2 km blocks on the Canadian Coast Guard research vessel *W.E. Ricker*, or a chartered industry vessel. These data are available under an Open Government License and can be accessed online (https://open.canada.ca/data/en/dataset/557e42ae-06fe-426d-8242-c3107670b1de).

The trawl survey recorded the total catch (number of individuals) of animals found in each tow. For each trawl tow that recorded *S. fragilis*, we determined the total area (m^2) covered by multiplying the width of the trawl doors (m) by the distance covered (m). We then calculated the density of *S. fragilis* in each trawl by dividing the total number of *S. fragilis* caught in all trawls by the total area covered (indiv. m^{-2}). This information was used to calculate mean density for each survey year (2004–2018). For some tows, a catch weight (kg) was recorded without a corresponding catch count. In these cases we first calculated the average weight per piece based on catches that recorded both a count and weight. We then divided the recorded weight of catches with a missing count by the average weight per piece (Anderson et al., 2019). Bottom depth (m) was reported as the modal bottom depth for each trawl tow. For each survey year, we determined the upper and lower depth limits, the mean and median depth, and the upper and lower 25% quantiles of the depth distribution.

2.5. Data analysis

2.5.1. S. fragilis density and environmental predictor variables

We used generalized additive models (GAMs) to characterize temporal trends in urchin density, and model possible responses to environmental change within and between years. GAMs are an extension of generalized linear models that allow for non-linear trends to be modeled using smooth functions of covariates (hereafter "smoothers", Wood 2011). The mgcv package (Wood 2011) in R (R Core Team 2020) enables automatic estimation of smoothness parameters using a variety of algorithms (Wood et al., 2016). Here, we fit GAMs using Restricted Maximum Likelihood Estimation (REML) to select smoothness parameters, since it is generally considered to be the most stable compared to other fitting procedures (Wood 2011). To preserve the inherent count-distribution of the urchin abundance data, and to account for possible overdispersion (Zuur et al., 2009), we fit all urchin density models with a negative-binomial distribution and log-link function. We also included the camera field of view (m^2) as an offset term to standardize abundance to density and account for differences in the FOV between years.

To determine within- and between-year trends in urchin density, we first modeled the data using only sampling time (ST) and sample year as covariates (see Appendix 2 for details). The estimated smoother for ST detrends the data, making the residuals a stationary process; thus, in this case, modeling urchin abundance as a smooth function of ST and year was sufficient to account for any temporal autocorrelation present in the video time series (Fig. S1). We selected the best temporal model using Aikike's Information Criteria (AIC, Burnham et al., 2002). Finally, we added global smooths of dissolved oxygen, BBLc magnitude, and ADCP backscatter (as a proxy for particulate organic matter; Chanson et al., 2008) to the best temporal model to determine average *S. fragilis* response to environmental change (Table 3). Including temporally-correlated environmental covariates in a model that already has a smoother for time requires that the environmental smoothers explain variation above and beyond the temporal smooth (Hayes et al., 2020). After fitting models, we tested for concurvity, the ability of a smooth function of one variable to be reconstructed by the smooth function of another variable; essentially the nonlinear analogue of collinearity (Buja et al., 1989; Morlini 2006).

To investigate how the 2013–2016 warm blob altered ocean dynamics, in particular benthic dissolved oxygen concentrations, we also fit a separate Generalized Additive Mixed-Model (GAMM) to model changes in benthic dissolved oxygen at BCUS over the entire study period (2013–2020). GAMM allows explicit specification of temporal autocorrelation structures (Lin and Zhang 1999) and allowed us to model seasonal and interannual variation and account for residual temporal autocorrelation not captured by the covariates. For the temporal model, we included a smooths for ST and day of year (WoY), and a year-level random effect smooth. We also included an autoregressive (AR) correlation structure that allowed the previous two terms to be correlated with the response, known as AR (2), which was chosen by comparing models with different temporal dependence structures using an Analysis of Variance (Table S1), and by comparing residual autocorrelation plots (Fig. S3). After we determined the best fitting temporal model, we then included global smooths of surface chlorophyll-*a* and SSTa to determine their influence on benthic oxygen over time. For these models, benthic oxygen and SSTa were binned to an 8-day average to align with the sampling frequency of chlorophyll-*a*. We followed the same model specification and selection procedures outlined above.

We also fit another GAMM to model the relationship between surface chlorophyll-*a* and sea-surface temperature anomalies over the entire study period (2013–2020). We modeled log-transformed surface chlorophyll-*a* (to meet distribution assumptions in residuals) as a function of smooths of month of year and SSTa, with a year as a parametric fixed-effect and an AR (1) correlation structure. This allowed us to further examine the effect of "The Blob" on surface productivity, and how food export to the seafloor may have been affected. We followed the same model specification and selection procedures outlined above.

2.5.2. Trawl surveys

To examine changes in *S. fragilis* density and depth distribution over time, we first tested for normality using the Shapiro-Wilk normality test in R (Shapiro and Wilk 1965). Both density and capture depth violated the assumption of normality, so we used non-parametric tests to determine differences between survey years. We used the Kruskal-Wallis Rank Sum test (Kruskal and Wallis 1952) to test for differences in mean density across sample years, and Dunn's rank comparisons post-hoc test (Dunn 1964) with Bonferroni correction for multiple comparisons from the PMCMRplus package (Pohlert 2021) in R to determine in which years *S. fragilis* density differed on the continental margin. We used the Komolgorov-Smirnov test (Conover 1971) to test for differences in the distribution of capture depth between pairs of survey years, as well as between trawls where *S. fragilis* was captured and all trawls conducted to account for the possibility that any changes in depth distribution were caused by differences in trawling depth. We then used linear regression to determine how strong the relationship was between each depth parameter (upper and lower limits, mean and median depth, and 25% and 75% quantiles) and time.

Table 3
Akaike Information Criteria (AIC) table comparing Generalized Additive Model fits for Barkley Canyon Upper Slope urchin density. ΔAIC refers to the difference in AIC between each model and the best model for Temporal models and Temporal + environmental covariate (Env. Cov.) models. Global smooths in Temporal model + Env. Cov. are dissolved oxygen, current magnitude, and ADCP backscatter.

Model	df	AIC	ΔAIC
Temporal models			
G: density ~ s (Time) + $Year_i$	16	9556	1015
I: density ~ s $(Time)_{Year}$ + $Year_i$	43	8541	0
S: density ~ s (Time, Year) + $Year_i$	43	8832	291
GS: density ~ s (Time) + s (Time, Year) + $Year_i$	43	8823	282
GI: density ~ s (Time) + s $(Time)_{Year}$ + $Year_i$	43	8544	4
Temporal model + Env. cov.			
I + s (Oxygen) + s (Magnitude) + s (Backscatter)	39	7619	0
GI + s (Oxygen) + s (Magnitude) + s (Backscatter)	48	7624	5

All code and data used in this paper are available at: https://github.com/rjcommand/bcus-urchin-dynamics.

3. Results

3.1. Temporal patterns of urchin density

S. fragilis was observed in 1245 out of 2228 videos (56%). Urchin density was highly variable over time, ranging from 0 to 61 indiv. m^{-2} (Fig. 2). Temporal patterns of density within years were characterized by extended periods of zero or few urchins followed by pulses of greater density (>2 indiv. m^{-2}) lasting between a few days and a few weeks, then returning to low density (Fig. 1). In 2013–2014, *S. fragilis* densities showed four distinct peaks, in late-September-early-October, mid-October, late-November, and late January. In 2014–2015, we observed two density peaks, at the beginning and end of September. In 2018, we observed four to five density peaks at the end of August-beginning of September, end of September (this might be two pulses that blur together), mid-October, and mid-November. Unfortunately, this time-series ends on November 23, 2018, and no video data are available for winter 2018. In 2019–2020, there were three to four density peaks; mid-November, mid-December, and end of December to mid-January (this might be two pulses that blur together).

Between years, *S. fragilis* displayed the lowest densities during the marine heatwave in 2014–2015 (0.157±0.012 indv. m^{-2}) and in 2018 (1.283±0.131 indv. m^{-2}) shortly after the heat anomaly had subsided. The highest average densities occurred in 2019–2020 (2.104± 0.21 indv. m^{-2}) and in 2013–2014 (1.691±0.216 indv. m^{-2}) well after the cessation of, and at the very onset of the marine heat wave, respectively.

3.2. Pink urchin density model fit/model selection

GAMs that allowed the temporal trend in urchin density to vary by year (models I, S, GS, and GI) performed better than the model that included only a global smooth for sampling time, ST (model G) (Table 3). The best temporal model was model I, which allowed each year-level smooth of ST to have its own wiggliness penalty (Table 3). Adding environmental covariates improved model performance, and once again model I had the best fit with a global smooth for dissolved oxygen, bottom current (BBLc) magnitude, and ADCP backscatter (Fig. 3; Table 3). Higher values of dissolved oxygen (>1.23 mL/L, Fig. 3A) were linearly associated with higher urchin densities, while lower urchin densities were linked to high levels of backscatter (Fig. 3B). Urchin density was also negatively associated with the global smooth of BBLc magnitude (i.e. a negative effect of fast-moving currents on urchin densities), however this term did not result in any significant

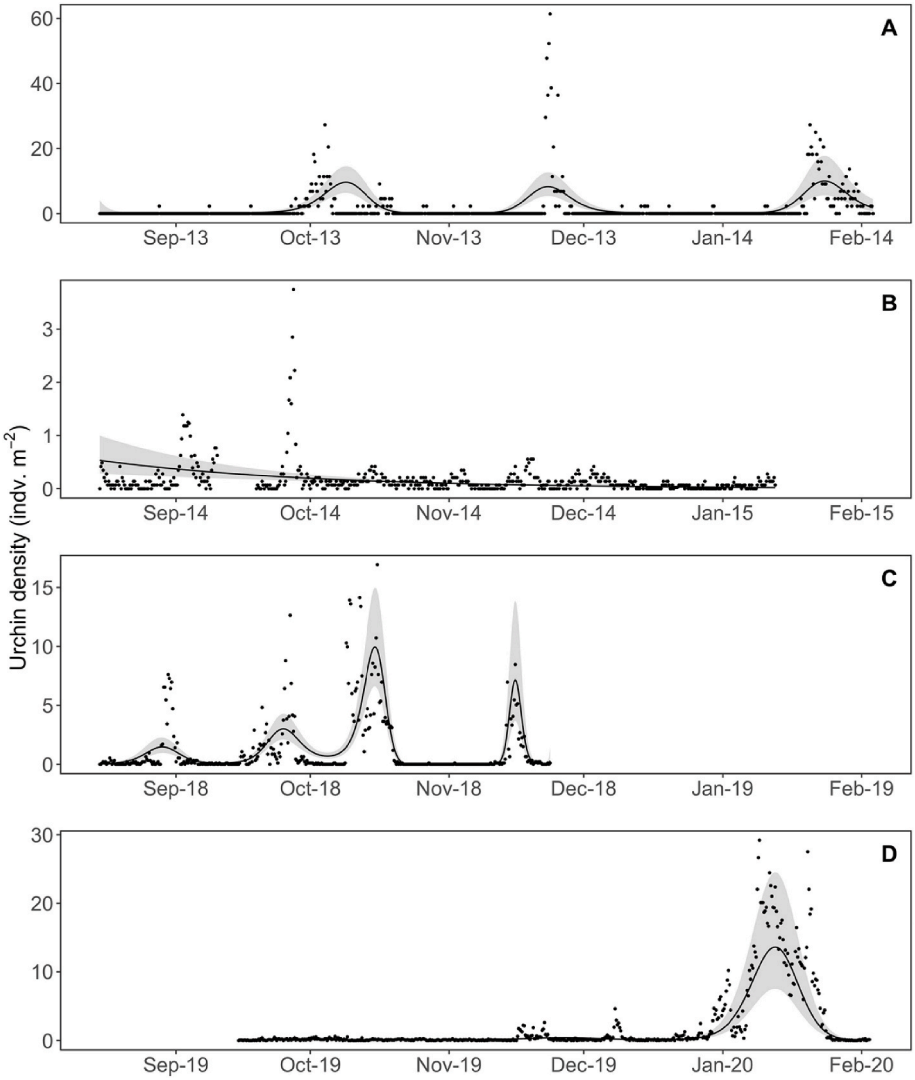

Fig. 2. Observed pink urchin density (points) and predicted (solid lines) values from the highest-ranking generalized additive model for urchin density (model I + env, see Tables 3 and 4). Solid lines are the smooth mean trend of urchin density for each year, the ribbon is ± pointwise 95% confidence interval.

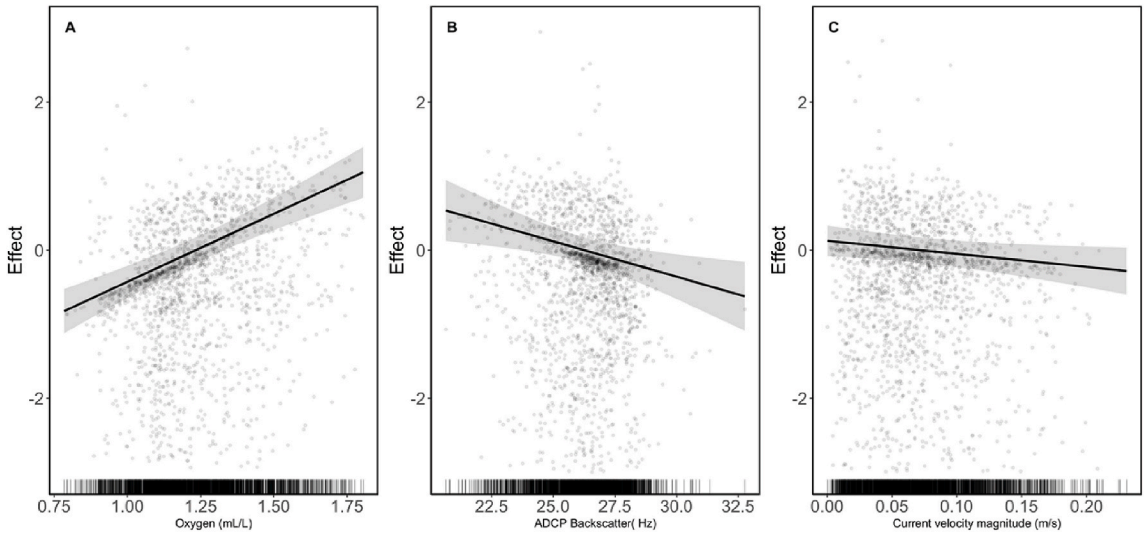

Fig. 3. Global smooths for the effects of oxygen (A) and ADCP backscatter (B) on *S. fragilis* density from the final temporal and environmental covariate GAM. Points represent model residuals and highlight variation around the average effect for each environmental term in the highest-ranking generalized additive model for urchin density (model I + env, see Tables 3 and 4).

improvements to the final model (p = 0.035, Fig. 3c, Table 4). Although this term is statistically significant, caution is warranted when interpreting marginally significant smooth terms in GAMs as p-values are calculated without considering the uncertainty in estimating smoothing parameters (Wood et al., 2016).

The final model that included temporal and environmental smooths resulted in strong coherence (R^2 = 0.739) between observed and predicted values for 2019–2020 (Fig. S3). However, the model is conservative at high urchin densities in early years, consistently underpredicting in 2013–2014 and 2014–2015 (Fig. S3). The model underfit extreme values of urchin densities and over-predicts a run of zeros in 2018 but does well at moderate densities that characterized most of the time series.

3.3. Environmental models

3.3.1. Seafloor dissolved oxygen GAMM

Dissolved oxygen concentration (hereafter, [DO]) near the seafloor at BCUS varied seasonally and interannually, ranging from 0.80 to 1.89 mL/L (Fig. 4). [DO] increased from 2013 until early 2016 commensurate with the onset and duration of the marine heat wave that affected the study area (Fig. 4). The GAMM fit for weekly benthic oxygen as a function of ST, day of year, surface chlorophyll-*a*, and sea-surface temperature anomaly provided a good fit to the dissolved oxygen time series (R^2_{adj} = 0.707, Fig. 4). Benthic [DO] varied seasonally, with low oxygen in summer and high oxygen in autumn and winter across years (Fig. 5A). Benthic [DO] was negatively associated with surface chlorophyll-*a* concentration throughout our study period (Figs. 5B and 6, Table 5). [DO] was below the 2013–2020 mean on average when surface chlorophyll-*a* was greater than 2.5 mg m^{-3} (Fig. 6). A statistically significant, non-linear temporal trend in seafloor [DO] was also observed (Fig. 5C), where [DO] peaked in early 2016 at the end of the MHW. A negative relationship of benthic oxygen and sea-surface temperature anomaly was also evident in the GAMM (Fig. 5D); however, this relationship was not statistically significant.

Table 4
Model summary table for parametric and smooth terms of final generalized additive model for urchin density at Barkley Canyon Upper Slope.

Parametric term	Estimate	Std. Error	Z Value	P-Value
(Intercept)	−1.936	0.442	−4.378	<0.001
Smooth terms	EDF	Ref DF	Chi.sq	P-Value
s (sample_time):Year 2013–2014	10.31	10.859	222.089	<0.001
s (sample_time):Year 2014–2015	1.002	1.004	114.33	<0.001
s (sample_time):Year2018	10.891	10.994	411 .33	<0.001
s (sample_time):Year 2019–2020	9.407	9.839	852.897	<0.001
s (Year)	1.706	3	37 .386	<0.001
s (Oxygen)	1	1.000	46.304	<0.001
s (Magnitude)	1.001	1.001	4.466	0.035
s (Backscatter)	1.001	1.002	8.012	0.005
Parametric term	Estimate	Std. Error	Z Value	P-Value
(Intercept)	−1.936	0.442	−4.378	<0.001
Smooth terms	EDF	Ref DF	Chi.sq	P-Value
s (sample_time):Year 2013–2014	10.31	10.859	222.089	<0.001
s (sample_time):Year 2014–2015	1.002	1.004	114.33	<0.001
s (sample_time):Year2018	10.891	10.994	411 .33	<0.001
s (sample_time):Year 2019–2020	9.407	9.839	852.897	<0.001
s (Year)	1.706	3	37 .386	<0.001
s (Oxygen)	1	1.000	46.304	<0.001
s (Magnitude)	1.001	1.001	4.466	0.035
s (Backscatter)	1.001	1.002	8.012	0.005

3.3.2. Surface chlorophyll-a GAMM

GAMM revealed seasonal changes in surface productivity above BCUS, with high chlorophyll-*a* concentration observed in late Spring and Summer and low chlorophyll-*a* concentration in the Autumn and Winter (Fig. 7A). We also detected a negative, non-linear relationship between chlorophyll-*a* and warm-water anomalies (Fig. 7B).

3.4. Trawl survey data (2004–2018)

From 2004 to 2018, approximately 7478 *S. fragilis* were caught in the benthic trawl surveys. We found statistically significant differences in mean S. fragilis density between sampling years (Table 6), however we did not find evidence of a decline in the mean S. fragilis density off Vancouver Island over the study period (2004–2018) or during the MWH (Fig. 7). However, S. fragilis density was highly variable, which may be indicative of their patchy distribution on the continental margin.

The depth distribution of *S. fragilis* changed across the survey years (Fig. 9, Table 6.). The upper limit of *S. fragilis* shoaled from 119.0 m to 70.0 m at a rate of 3.5 m yr^{-1} on average (Fig. 10A). The upper 25% quantile of *S. fragilis* depth distribution also shoaled from 144.5 m to 116.0 m, a rate of 2 m yr^{-1} on average, and exhibited lower variability than the upper limit (Fig. 10B). Additionally, the median of S. fragilis depth distribution shoaled from 170.75, to 141.0 m, a rate of 2.16 m yr-1 on average (Fig. 10F). A two-sample Komolgorov-Smirnov (K–S) test

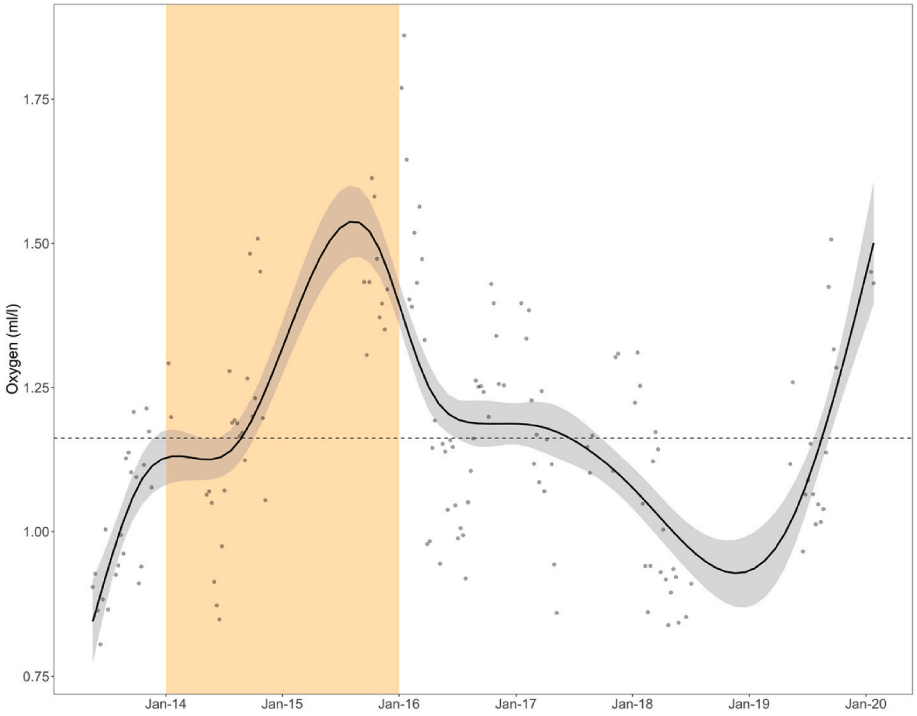

Fig. 4. Weekly dissolved oxygen concentration (points) at Barkley Canyon Upper Slope from 2013 to 2020, with fitted model to investigate how oxygen varied over time in relation to surface chlorophyll-*a* and sea surface temperature anomalies. Solid black line is the smoothed model predictions of oxygen over time, conditional on the generalized additive mixed model (Table 5). The grey ribbon is ± standard error around the trend, and horizontal dashed line is the mean dissolved oxygen across the entire study period. Orange shaded area represents the duration of the 2013–2016 marine heatwave.

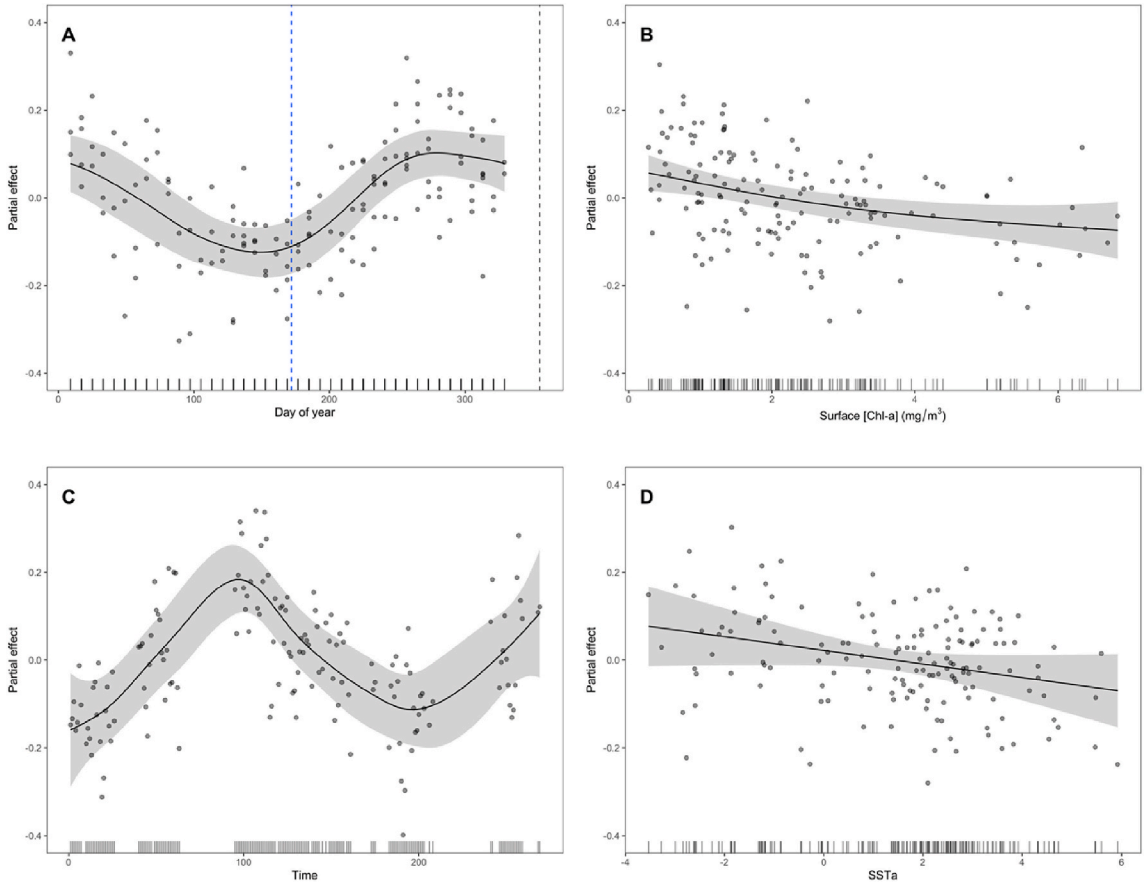

Fig. 5. Effect smooths from the oxygen GAMM. Smooth effects of day of year (A) and surface chlorophyll-a concentration (B), time (C), and sea-surface temperature anomaly (D). Solid black lines represent effect of the covariate on oxygen concentration, grey ribbons are ± 95% confidence interval around the mean. Statistically significant positive or negative effects of each covariate on oxygen concentration occur when the ribbon does not include a partial effect of 0. Vertical dashed lines in (A) are the average day of the onset of summer (blue) and winter (grey).

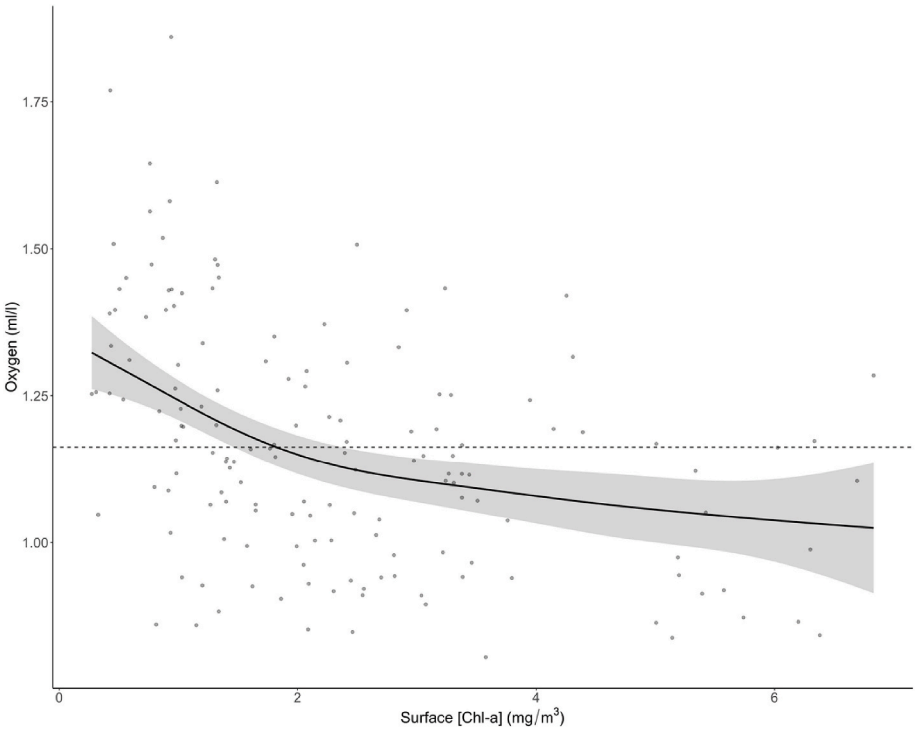

Fig. 6. Predicted values of oxygen for weekly surface chlorophyll-a concentration on benthic dissolved oxygen at Barkley Canyon Upper Slope across the entire study period (2013–2020). Points are a scatter plot of dissolved oxygen and chlorophyll-a, solid black line is the smooth effect, grey ribbon is ± 95% CI around the smooth. Horizontal dashed line is the mean dissolved oxygen concentration across the entire study period.

Table 5
Model summary table for parametric and smooth terms of final generalized additive mixed-model for benthic dissolved oxygen at Barkley Canyon Upper Slope.

Parametric term	Estimate	Std. Error	Z Value	P-Value
(Intercept)	1.007	0.043	23.348	<0.001
Smooth term	EDF	Ref DF	Chi.sq	P-Value
s (Time)	5.397	5.397	6.913	<0.001
s (Week of year)	5.274	10	6.885	<0.001
s (Chlorophyll-a)	1	1	8.88	0.003
s (SSTa)	1	1	2.781	0.097

indicated that the upper and lower limits, 25% quantile, and median of *S. fragilis* depth distribution come from a different probability distribution than the same parameters measured in all species trawls (Table 7). The linear regression results further indicated the shoaling trends in upper limit, 25% quantile, and median are only present in the *S. fragilis* trawls and is absent from the all-species trawls (Fig. 10A, B, F, Table 7). A two-sample K–S test also indicated that the lower limit of *S. fragilis* differs from the all-species trawls, however this was not corroborated by the linear regression (Table 7, Table 8). The 75% quantile, lower-limit, and mean depth also appear to shoal over time, though these trends were not statistically significant and were indistinguishable from the trend in all trawls (Fig. 10C–F, Table 7).

4. Discussion

Pink urchin densities varied within and between years at the Barkley Canyon Upper Slope (BCUS) site, with lower densities following the 2013–2016 NEP marine heat wave anomaly (MHW) or the so-called warm "Blob" (Kintisch 2015), and recovery to pre-blob levels in 2018. *S. fragilis* densities were positively associated with dissolved oxygen concentration across all years, with this variable fluctuating both seasonally and interannually. Dissolved oxygen was negatively associated with surface chlorophyll-*a* concentrations, which, in turn, was negatively associated with the sea-surface temperature anomalies recorded during the period of abnormally high temperatures in the NEP. By contrast, ADCP backscatter (as a proxy for particulate organic matter) was negatively associated with *S. fragilis* density. Together, these results suggest *S. fragilis* density at BCUS is mediated by two controlling variables – food availability and oxygen, which are in turn influenced by ocean warming, coastal upwelling dynamics, and local hydrodynamics.

The broad-scale environmental shifts caused by the 2013–2016 MHW, with remarkable effects over ecosystem functioning and productivity, have been well described elsewhere (Cavole et al., 2016; Yang et al., 2018). However, its effects on deep-sea benthic ecosystems and community structure have only been addressed in a single study at the long-term abyssal monitoring Station M off the California Margin (Kuhnz et al., 2020). Our results indicated a complex interplay of environmental control over *S. fragilis* population by a concert of variables that ultimately regulate food availability and metabolic acclimation under nearly permanent hypoxic conditions in the slope offshore Vancouver Island. The combination of our observatory and bottom trawl survey data seems to corroborate a recent study that showed that *S. fragilis* is undergoing habitat expansion, extending its range upslope and over the shelf following the shoaling of the NEP OMZ (Sato et al., 2017). Under low dissolved oxygen concentrations (13–42 μmol kg^{-1}) found at the OMZ core (450–900 m) off the California margin, *S. fragilis*, experience drastic reduction in reproductive fitness expressed in terms of suppressed gonadal development (Sato et al., 2018). In addition, the Sato et al. study pointed to reduced hardness and stiffness of the calcitic endoskeleton coupled with increased porosity and pore size in individuals collected in these same OMZ core areas, which are also characterized by low pH, ranging from 7.57-7–59 (Sato et al., 2018). The authors therefore predicted that *S. fragilis* may be potentially vulnerable to crushing predators if these conditions of warming, acidification and deoxygenation become more widespread in the future.

The bottom trawl survey data covering an area of 760 km^2 and a depth gradient of nearly 400 m indicated *S. fragilis* has expanded into

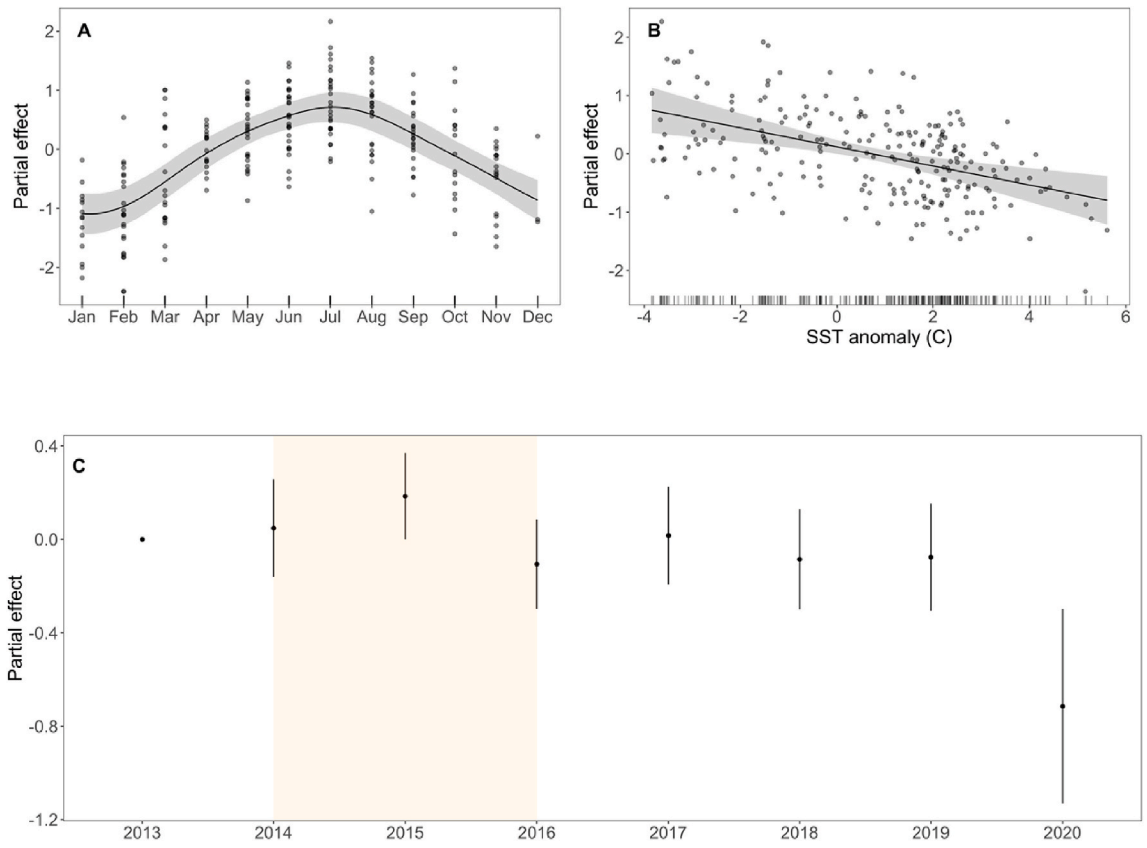

Fig. 7. Smooth effects of month of year (A) and sea-surface temperature anomaly (B) from the generalized additive mixed model for chlorophyll-*a*. Points represent model residuals and highlight variation around the average effect for each smooth covariate in the model chlorophyll-a model. Solid lines are the mean effect of the covariate on chlorophyll-a concentration, grey ribbons are ± 95% confidence interval around the mean. Parametric fixed-effect of year (C), points are the mean effect of each year relative to 2002, vertical lines are ± 95% confidence interval around the mean effect. Orange shaded area represents the duration of the 2013–2016 marine heatwave, known as "The Blob".

shallower water at a rate of 2.0 m yr^{-1} from 2004 to 2018 (Figs. 9 and 10), similar to the shoaling documented in Sato et al. (2017). In contrast to Sato et al. (2017), the lower limits of pink urchin depth distribution in the upper 400 m off Vancouver Island remained stable over time, suggesting range expansion into favourable conditions rather than range shifting away from a physiological limit, although deeper trawls are needed to investigate the lower limits of *S. fragilis* depth range in this region of the NEP. Interestingly, the trawl survey data did not indicate a decline in *S. fragilis* density on the continental shelf between 2004 and 2018, including during and following the 2013–2016 MHW. Thus, the highly mobile nature of S. fragilis may have contributed to its survival on the continental shelf despite the threat of food limitation imposed by the MHW. However, while the MHW did not appear to cause of pink urchin density decline on the continental shelf off Vancouver Island, the decimation of coastal kelps and other macroalgae may inhibit its survival, and recruitment through food limitation in the future (Sato et al., 2018; Starko et al., 2019; McPherson et al., 2021).

4.1. Within- and between-year variation of urchin density

S. fragilis is a detritivore that feeds on fresh phytodetritus, kelp and other macroalgae detritus, and other organic matter on the seafloor, and it forms large feeding aggregations on the continental slope (Booloottian et al., 1959; De Leo et al., 2017; Campanyà-Llovet et al., 2018). Within each year, we observed alternating periods of few (0–1 indiv. m^{-2}) urchins and "spikes" of many (2 > indv. m^{-2}) urchins, which likely reflect the patchy distribution of food on the continental slope. We also observed large aggregations of *S. fragilis* around small seafloor depressions (R.C., pers obs.) that likely promoted patchiness in the accumulation of organic matter (Campanyà-Llovet et al., 2018). This patchy distribution pattern is consistent with observations from previous studies of *S. fragilis* on continental margin settings off British Columbia (De Leo et al., 2017; Campanyà-Llovet et al., 2018) and further south at the Oregon margin (Sumich and McCauley 1973).

Observed sea urchin density patterns could also be an artifact of differences in activity levels within or between sampling days, whereby higher (lower) mobility during certain times could inflate (depress) the interpreted density – a common issue in time-lapse imagery studies (Aguzzi and Company 2010). In the present study, we noted one period of high mobility (R.C. pers obs.) at the end of 2019 (Fig. 2D), in which a large aggregation of urchins moved through the field of view over a three-week period. We sampled at four evenly spaced intervals throughout a 24-h period each day, and during a similar seasonal period across years to minimize bias due to differences in activity levels related to the day-night or seasonal cycles. However, we cannot fully constrain the effect of activity levels on density estimates with a single fixed camera. Thus, density estimates from the platform should be considered in the context of the visible field of view, while density patterns observed in the trawl survey data are more representative of the continental shelf.

Sea urchins are important for nutrient cycling through locomotion and bioturbation, and consumption of detritus (Booloottian et al., 1959). Indeed, large aggregations of feeding urchins can influence the spatial distribution and patchiness of nutrients on the continental margin (Campanyà-Llovet et al., 2018). *S. fragilis* may preferentially feed on high C:N ratio patches, and directly influence the composition of nutrients in the sediment (Campanyà-Llovet et al., 2018), while locomotion by pink urchins contribute sediment-surface reworking rates

Table 6
Dunn's post-hoc multiple comparisons with Bonferroni correction for S. fragilis density over time from the West Coast Vancouver Island synoptic bottom trawl surveys. Komolgorov-Smirnov (K–S) comparison of S. fragilis depth distributions for each pair of survey years. Bold rows indicate statistical significance at the α = 0.05 level.

Comparison	Dunn's P-value	K–S Test statistic	K–S P-value
2016 vs 2018	1	0.187	0.177
2014 vs 2018	1	0.136	0.42
2014 vs 2016	0.808	0.102	0.855
2012 vs 2018	1	0.281	0.002
2012 vs 2016	0.273	0.158	0.34
2012 vs 2014	1	0.209	0.057
2010 vs 2018	0.007	0.267	0.05
2010 vs 2016	0.989	0.173	0.485
2010 vs 2014	0.001	0.164	0.485
2010 vs 2012	<0.001	0.203	0.22
2008 vs 2018	1	0.270	0.017
2008 vs 2016	1	0.166	0.395
2008 vs 2014	0.456	0.167	0.318
2008 vs 2012	0.146	0.149	0.441
2008 vs 2010	1	0.118	0.918
2006 vs 2018	1	0.308	0.004
2006 vs 2016	0.37	0.198	0.21
2006 vs 2014	1	0.193	0.19
2006 vs 2012	1	0.189	0.177
2006 vs 2010	<0.001	0.104	0.95
2006 vs 2008	0.209	0.095	0.94
2004 vs 2018	1	0.440	0.001
2004 vs 2016	1	0.314	0.063
2004 vs 2014	1	0.329	0.034
2004 vs 2012	1	0.196	0.429
2004 vs 2010	0.027	0.256	0.259
2004 vs 2008	1	0.236	0.28
2004 vs 2006	1	0.269	0.158

Table 7
Exact two-sample Kolmogorov-Smirnov tests for differences in depth distribution parameters between West Coast Vancouver Island benthic survey trawls that caught Strongylocentrotus fragilis urchins and all trawls. Null hypothesis is that there is no difference in depth distribution parameters between trawls.

Distribution parameter	D	P-value
Upper limit	1	<0.001
25% Quantile	1	<0.001
Mean	0.25	0.9801
Median	0.875	0.002
75% Quantile	0.5	0.2827
Lower limit	0.875	0.002

between 15.1 and 21.0 m^2 yr^{-1} at the BCUS site (Robert and Juniper, 2012). Their locomotion and feeding aggregations also change the distribution and mixing depth of nutrients within sediments, which affects infaunal communities that are also key for nutrient cycling (Campanyà-Llovet et al., 2018). Locomotion by sea urchins has also been shown to influence oxygen circulation in sediment pore water (Vopel et al., 2007), affecting sediment redox potential and nutrient flux at the sediment-surface interface (Morford and Emerson 1999). All these processes release essential nutrients into the water column, which contribute to surface and coastal productivity. As warming events become more common and deoxygenation continues (Whitney et al., 2007; Pierce et al., 2012; Ross et al., 2020), the density and distribution of *S. fragilis* is likely to change, with direct consequences for biogeochemical cycling on the continental margin.

We found a positive relationship between *S. fragilis* density and dissolved oxygen concentration across all years. Previous studies have documented changes in *S. fragilis* distribution commensurate with the shoaling OMZ in the Southern California Bight (Sato et al., 2017), suggesting a tolerance to low oxygen. Similarly, De Leo et al. (2017) found *S. fragilis* distributed from 300 m to 1400 m depth along the continental slope near BCUS, a range that includes the OMZ. However, aside from high density (>50 indiv./500 m) feeding aggregations observed between 500 and 600 m at the edge of the OMZ, *S. fragilis* density was up to 2 orders of magnitude higher outside the OMZ (DO ~ 1.4 mL/L) than inside the OMZ (DO < 0.5 mL/L; De Leo et al., 2017). This suggests that *S. fragilis* can tolerate low oxygen, but still does prefer a higher oxygen environment, which agrees with previous studies describing a competitive advantage of *S. fragilis* over other less resilient shelf-inhabiting urchin species (Sato et al., 2017). Higher pink urchin densities also highlight a possible OMZ 'edge effect' proposed by Levin (2003), where benthic faunal densities may exhibit maximum near the upper and lower boundaries of OMZs at specific oxygen concentrations that may represent a physiological threshold or preference.

ADCP backscatter was negatively associated with *S. fragilis* density. If ADCP backscatter could be considered as a proxy for sinking organic matter (Chanson et al., 2008), a positive relationship of density with organic matter deposition on the seafloor would be expected. While many types of particles and organisms are detected in ADCP backscatter (Hoitink and Hoekstra 2005; Lara-Lopez and Neira 2008; Chanson et al., 2008; Dwinovantyo et al., 2017; De Leo et al., 2018; Haalboom et al., 2021), at least some of this backscatter is likely due to particle resuspension from sediment disturbance. Resuspension of phytodetritus and other particulate organic matter deposited on the seafloor can occur when bottom currents are between 0.08 and 0.16 m/s (Beaulieu 2003). Although our GAM analysis did not find any statistically significant evidence of a direct link between BBLc magnitude and *S. fragilis* density, phytodetritus resuspension is possible within the range of BBLc observed in our study (Fig. S3). Bottom trawling is also known to contribute to sediment resuspension and high turbidity in benthic habitats (Puig et al., 2014). Barkley Canyon is located near active fishing grounds, and there have been three major trawl collisions with the NEPTUNE observatory infrastructure over the last ~8 years. Furthermore, direct measurements of turbidity and chlorophyll-a by a vertical profiling system also connected to the NEPTUNE cabled observatory at BCUS, have shown that bottom nepheloid layer (BNL) detachments can be associated with bottom trawling activities in the area (Arjona-Camas et al., [in-press]). For detritivores that primarily feed on drifting macroalgae and other phytodetritus, like *S. fragilis* (Harrold et al., 1998), regular resuspension events could reduce opportunities for feeding on fresh organic matter, resulting in lower urchin densities. In late-summer and fall, fast currents of the of the California Undercurrent (CUC) that flow northwestward along the continental margin may be a significant source of particle resuspension and advection (Hickey 1979; Arjona-Camas et al., [in-press]), preclude organic matter deposition in the first place, forcing much of the sinking organic matter down-slope or into nearby submarine canyons (Baker and Hickey 1986). Indeed, the sediments at the head of Barkley Canyon (200 m) near our study site have the lowest quantity and quality of organic matter compared to sediments throughout the rest of the canyon (Campanyà-Llovet et al., 2018). In addition, from all NEPTUNE instrument platforms in Barkley Canyon and Upper Slope that possess a seafloor video camera, kelp macroalgae detritus is observed in much greater concentrations deeper in the slope at Barkley Node (620 m) and inside the canyon topography at Barkley MidEast (987 m) and Barkley Axis (970 m) (De Leo, FC, unpublished observations). The negative association of *S. fragilis* density with high ADCP backscatter may therefore be related to low organic matter deposition caused by fall storms, along-margin currents, and intense bottom trawling activity that contribute to high sediment resuspension and BNL formation at slope depths on the continental margin.

4.2. *S. fragilis* response to the 2013–2016 marine heatwave

We observed the highest urchin density before and well after the MHW in 2013–2014 and 2019–2020, and the lowest density of urchins during the MHW in 2014–2015 and following the MHW in 2018. The MHW has been reported to reduce overall productivity in the region.

Thermal stratification in the upper ocean reduced coastal upwelling (Leising et al., 2015; Tseng et al., 2017), surface primary productivity (McGowan 1998; Yang et al., 2018), and organic matter flux to the seafloor (Smith Jr. 1999; Smith et al., 2018). Additionally, the higher seafloor dissolved oxygen concentration we observed during the MHW indicates reduced upwelling of water from the OMZ (Barth et al., 2018), and lower respiration as a result of low food export to the seafloor (Drazen et al., 1998). The latter is also corroborated by the negative relationship between surface chlorophyll-*a* and benthic oxygen in our GAMM (Fig. 5). Hence, despite observing a positive relationship between *S. fragilis* and dissolved oxygen at BCUS, which would suggest that we could expect higher urchin density at BCUS during the MHW, the low density in 2014–2015 and in 2018 may be explained by lower than average or patchier food availability resulting in high urchin mobility or mortality.

If warming-induced thermal stratification reduced upwelling and food availability on the seafloor, we expect that the relative proportion of food settling at the upper slope may be lower compared to non-MHW years (Kuhnz et al., 2020). Consequently, *S. fragilis* may move down-slope in search of food, which could explain reduced density at BCUS during 2014–2015. ROV surveys that found higher *S. fragilis* densities outside the OMZ (De Leo et al., 2017) were conducted in early August, when food availability at the benthos was still high following the spring and summer phytoplankton blooms. Further, *S. fragilis* has been observed aggregating rapidly within the OMZ when macroalgal detritus is available (Yee et al., in preparation). Together with our findings, this suggests that *S. fragilis* may exhibit a foraging-respiration trade-off strategy - preferring higher oxygen in shallow water during autumn and early winter when food availability is low and migrating down-slope into the OMZ in late summer when food is plentiful. During the 2013–2016 MHW when oxygen at BCUS was highest (Fig. 4), dissolved oxygen concentration further down the slope was likely also higher than average, allowing *S. fragilis* to forage in deeper water for longer than under normal conditions. Observations of *S. fragilis* at the Barkley Node (643 m) have also demonstrated rapid aggregation on kelp falls, though these effects are masked by increasing dissolved oxygen (Connor Yee, pers. comm.). A video camera was added at the Barkley Node in August 2019 and is located just down-slope from the BCUS platform. These instrument platforms, spanning a depth gradient (400–620 m) on the slope adjacent to Barkley Canyon, could be used in concert during future studies to examine if *S. fragilis* is indeed more abundant in deeper water during warm-water anomalies.

Kelp export from the coast is a significant component of the diet of *S. fragilis* (Sato et al., 2018; Campanyà-Llovet et al., 2018). Kelp diversity and abundance in nearby Barkley Sound was significantly reduced following the 2013–2016 MHW (Starko et al., 2019), which would limit this food source on the continental slope. Kelp forests in some regions have been slow to recover following the MHW (McPherson et al., 2021), indicating possible long-term reduction of food export to the continental margin. Food limitation in the deep sea affects energy intensive processes like reproductive capacity and calcification rates (Sato et al., 2018), which influence recruitment and abundance of sea urchins (Zhao et al., 2013; Filbee-Dexter and Scheibling 2014). The ability of *S. fragilis* to calcify will likely be affected further under future ocean warming and acidification scenarios (McBride et al., 1997; Taylor et al., 2014), making them more vulnerable to crushing predators like crabs and fish (Sato et al., 2018; Asnaghi et al., 2020).

High mortality as a consequence of the MHW is another possible explanation for the low pink urchin densities observed in 2014–2015 and 2018. However, this explanation was not corroborated by the trawl survey data, which revealed significant temporal trends in the depth distribution, but not the density, of pink urchins across the continental slope off Vancouver Island. Although S. fragilis density appeared to decline from 2012 to 2016 (Fig. 8A, Table 6), densities remained within the range of variation observed across all other years. This high variability suggests that pink urchin distribution may be patchy on the scale of the continental shelf, consistent with the highly mobile nature of S. fragilis (Robert and Juniper 2012). Together, these observations suggest a mobility or migratory mechanism, rather than mortality, is likely responsible for the observed differences in pink urchin density at the BCUS platform.

4.3. Decadal distribution shifts (from bottom trawl surveys)

Although we did not observe a decline in dissolved oxygen at BCUS over the study period (2013–2020), previous studies in the NEP have documented deoxygenation and OMZ expansion on a decadal scale (Whitney et al., 2007; Pierce et al., 2012; Ross et al., 2020). Given our results and those of Sato et al. (2017, 2018), we expect *S. fragilis* distribution to shoal off Vancouver Island on a decadal scale as the OMZ

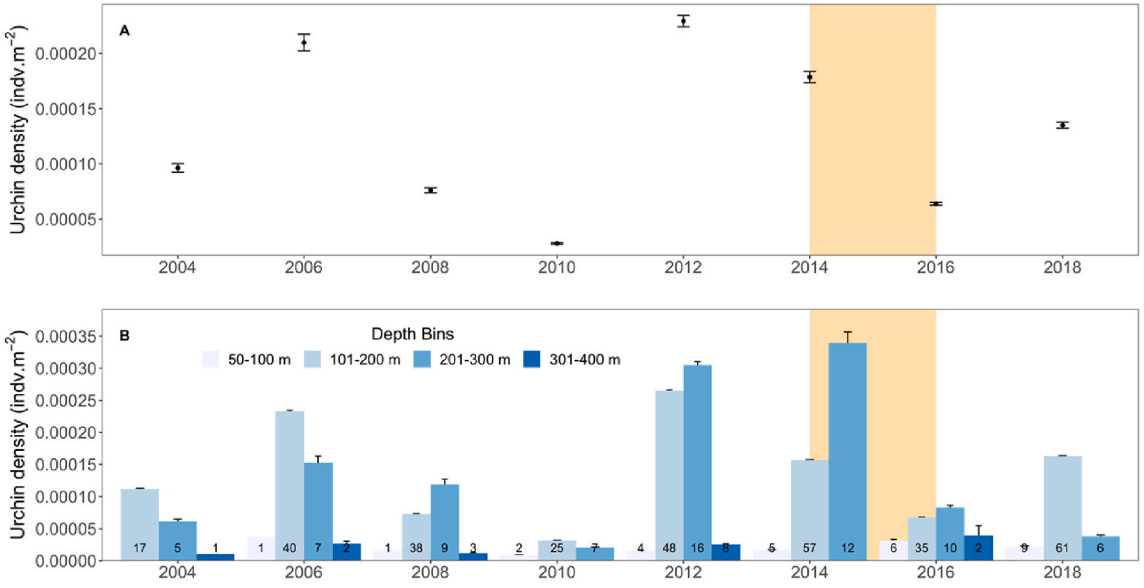

Fig. 8. Mean ± standard deviation of density of *S. fragilis* found in the West Coast Vancouver Island bi-annual trawl surveys from 2004 to 2018 considering the entire depth range of trawl samples (A) and by depth bin (B). Numbers in the bars represent the number of independent trawls used to calculate the mean. The orange band indicates the 2013–2016 "Warm Blob".

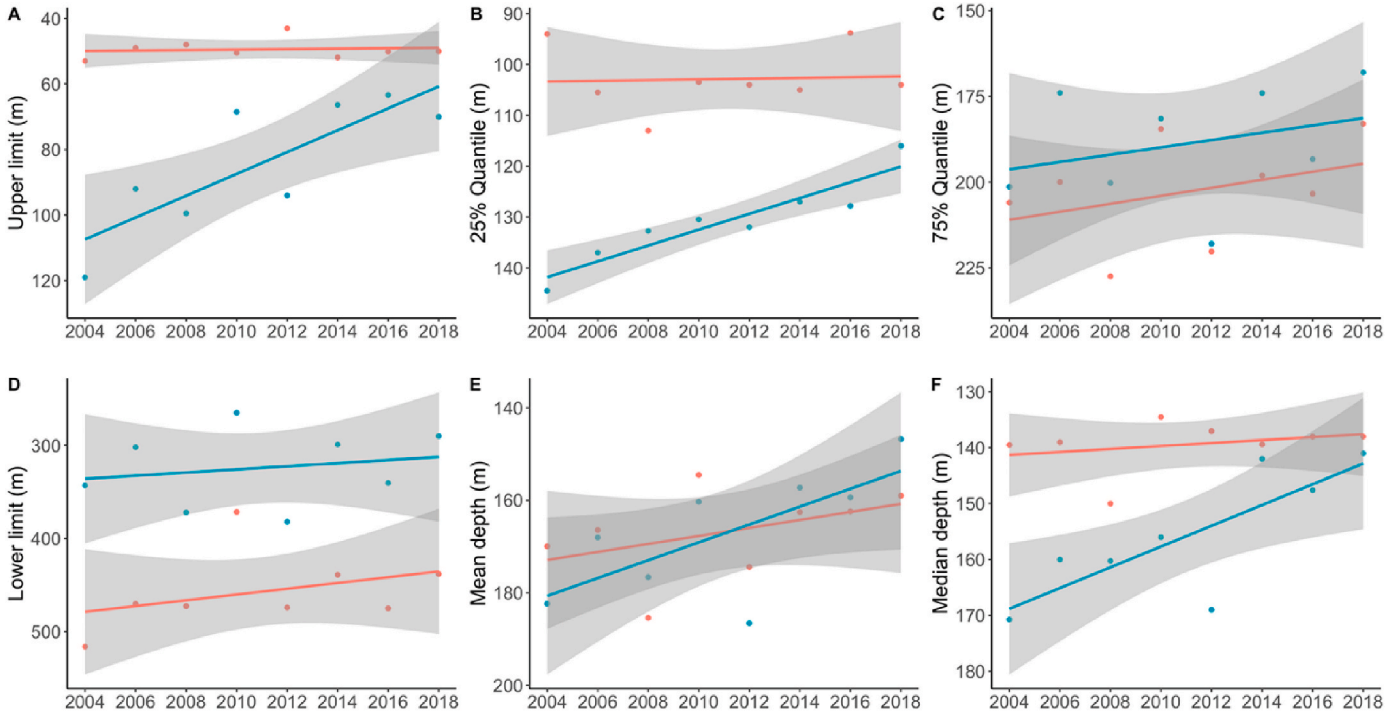

Fig. 9. Depth-distribution statistics from 2004 to 2018 from the West Coast Vancouver Island bi-annual trawl surveys for trawls where pink urchins were caught (blue points) and for all trawls (red points). Coloured lines represent the least squares fitted line for a simple linear model for all trawls (red line) and trawls where pink urchins were caught (blue line). Grey bands represent 95% confidence intervals around the fitted line.

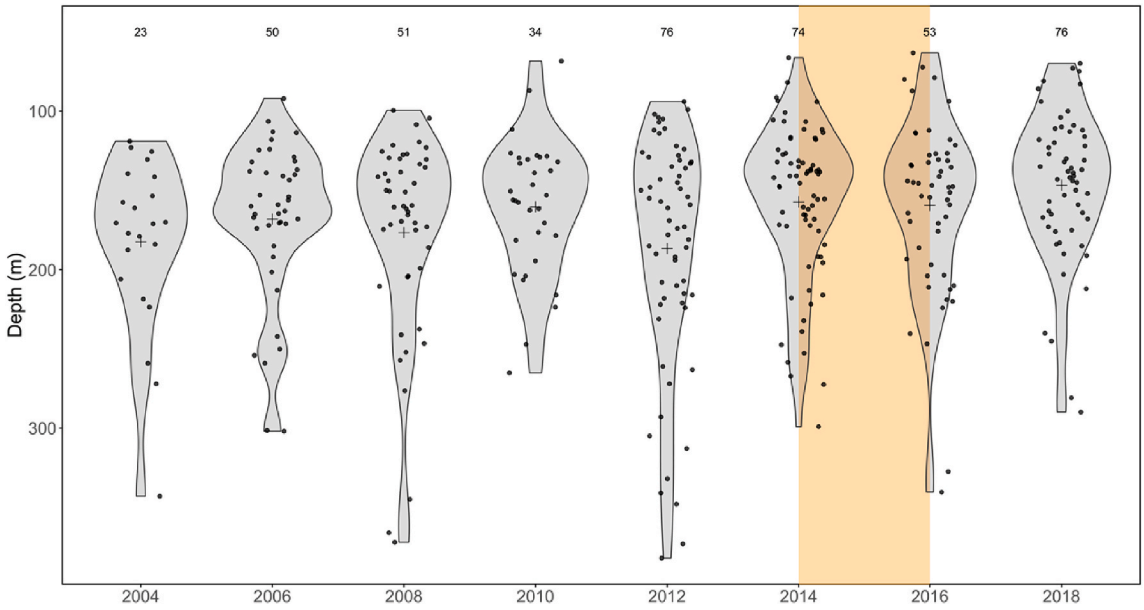

Fig. 10. Violin plot of depth distribution of S. fragilis obtained from the bi-annual West Coast Vancouver Island synoptic trawl survey from 2004 to 2018. Points indicate raw data and are jittered to better display the variation. + symbol indicates mean depth. Numbers above each box indicates the number of trawls in which S. fragilis was present for each survey year. Orange band indicates the 2013–2016 "Warm Blob". Two trawls found pink urchins at 800 m depth but were considered outliers and were subsequently excluded from analysis.

continues to expand. Interestingly, the observed shoaling of pink urchin upper limit and 25% quantile (Fig. 9) was not followed by a concomitant increase in pink urchin density (Fig. 8). This discrepancy may be explained by an overall decrease in pink urchin density on the shelf, which may have persisted due to the effects of the 2013–2016 MHW. The expected shoaling of pink urchins in response to deoxygenation will likely be modulated by the increasing prevalence, duration, and severity of warm-water anomalies that disrupt seasonal upwelling and food availability on the continental margin. The extent to which future SST anomalies may influence *S. fragilis* density and distribution should be considered to understand the consequences for coastal and deep-sea benthopelagic coupling in the NEP.

5. Conclusion

S. fragilis is a slow-moving calcifying organism and is susceptible to ocean change. Under future climate change scenarios, the distribution of *S. fragilis* on the continental margin may be affected - migrating into deeper water during periods of weak upwelling and shoaling over decades as deoxygenation continues. The density of *S. fragilis* may also be affected due to ocean warming disrupting food availability at the benthos, and acidification reducing their defense and reproductive capacity (Sato et al., 2018). This in turn may influence nutrient cycling on the slope, affecting infaunal community composition, biogeochemical cycling, and surface productivity. Long-term monitoring of the continental margin on multiple spatial and temporal scales is therefore critical to predict how these important marine ecosystems will respond to future ocean change.

Declaration of competing interest

The authors declare that they have no known competing financial interests or personal relationships that could have appeared to influence the work reported in this paper.

Data availability

Raw data are available at sites referenced in text. Processed data and code required to replicate analyses will made made available on GitHub (www.github.com/rjcommand/bcus-urchin-dynamics

Acknowledgements

Ocean Networks Canada is funded through the Canada Foundation for Innovation-Major Science Initiative (CFI-MSI) fund 30199. We are thankful for the support from ONC's marine and digital operations staff for servicing and maintaining the NEPTUNE observatory and for the curation and quality control of all oceanographic data streams used in this study. We also thank the Department of Fisheries and Oceans (DFO) and the Institute of Ocean Sciences (IOS), in Sidney, BC, Canada, for the publicly and freely available data from the long-term Line P monitoring program. RC was supported by an Early Career Faculty Award Grant to Dr. Katleen Robert from the Marine Environmental Observation, Prediction and Response Network (MEOPAR) and a Canada Research Chair (Ocean Mapping) to PI KR. We also thank M.E.C., J.A.M.M., P.K., K.C., S. N., A.J.C.S., and A. Y–S. for their feedback on early drafts of the manuscript.

Appendix A. Supplementary data

Supplementary data to this article can be found online at https://doi.org/10.1016/j.dsr.2022.103958.

Appendix 1. Field of view calculations

2013 field of view

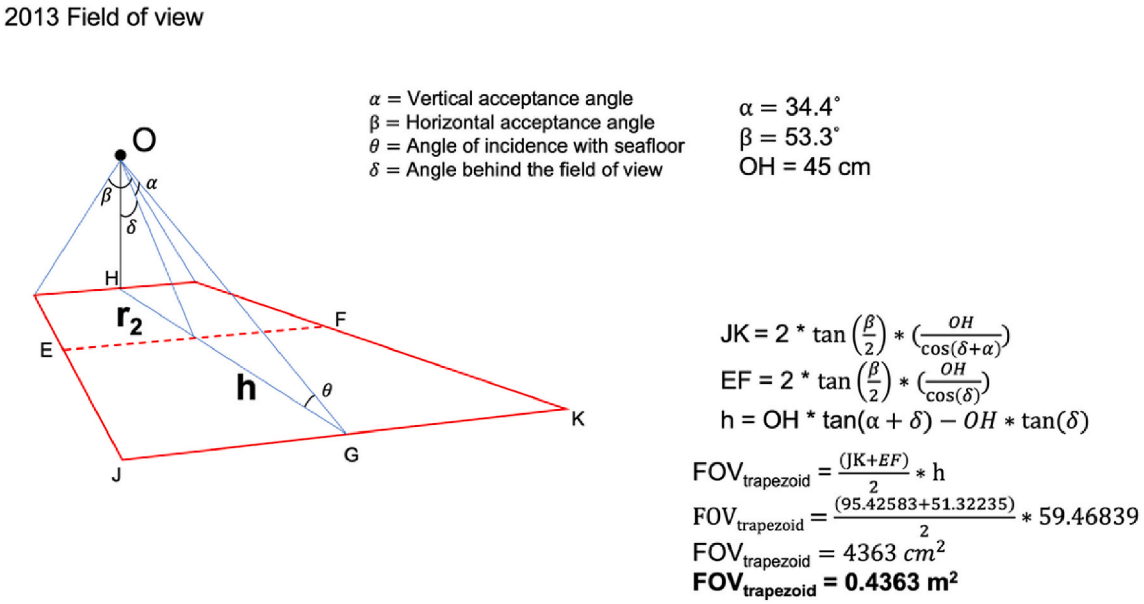

This field of view is calculated as the area of a trapezoid, where the width of the top and bottom are determined by doubling the tangent of one half the horizontal acceptance angle multiplied by the ratio of the camera height to the cosine of the angle incident with the camera lens at the top and bottom of the visible field of view (defined by the vertical acceptance angles. The calculated value was close to that reported in Chauvet (2018), so we used their previously published value of 0.5 m^2.

2014-2015 field of view

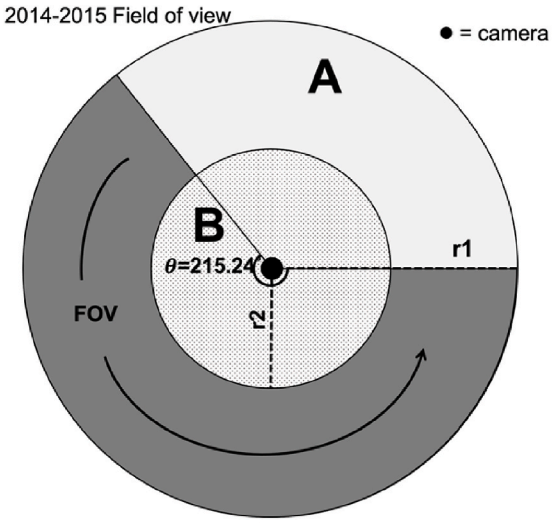

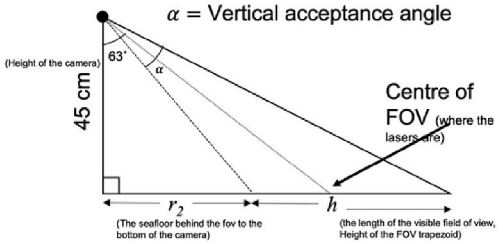

$r_2 = 45 * \tan(63 - \alpha/2)$

$r_1 = 45 * \tan\left(63 + \frac{\alpha}{2}\right)$

$h = r_1 - r_2$

$FOV_{circle} = (A - B) * \left(\frac{\theta}{360}\right)$

$A = \pi {r_1}^2 = \pi * (248.8533)^2 = cm^2$

$B = \pi {r_2}^2 = \pi * (47.17216)^2 = cm^2$

$FOV_{circle} = (248.8533 - 47.17216) * \left(\frac{215.24}{360}\right) = 112141\ cm^2$

FOV_{circle} = 11.2141 m²

The area covered by the 215.24° pan angle can be calculated by subtracting the area of a large circle by the area of a small circle (non-visible area), where the radius of the large circle is defined by the camera height multiplied by tangent of the known fixed tilt angle of the camera plus one half the vertical acceptance angle, and the area of the small circle is defined by the camera height multiplied by tangent of the known fixed tilt angle of the camera minus one half the vertical acceptance angle. The difference between the large and small circle leaves the visible area of the seafloor for a 360° pan. This area is multiplied by the fraction of a circle corresponding to the total pan angle (215.24°/360°) to get the fraction of the total area that is visible to the camera.

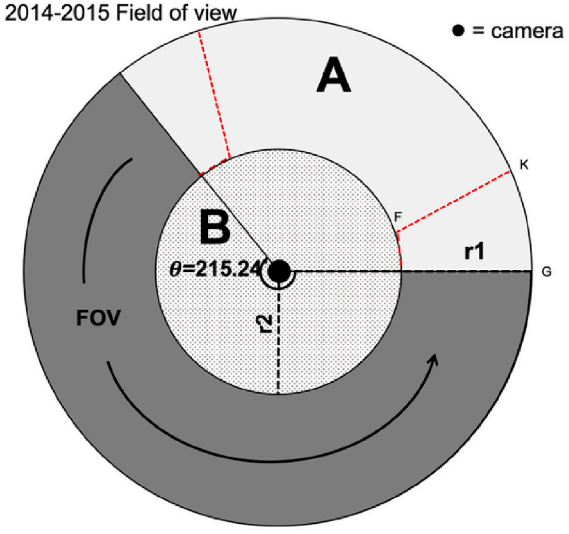

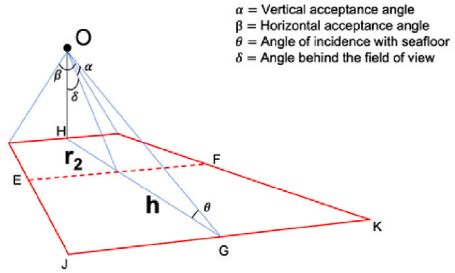

$JK = 2 * \tan\left(\frac{\beta}{2}\right) * \left(\frac{OH}{\cos(\delta+\alpha)}\right)$

$EF = 2 * \tan\left(\frac{\beta}{2}\right) * \left(\frac{OH}{\cos(\delta)}\right)$

$h = r_1 - r_2$

$FOV_{trapezoid} = \frac{(JK+EF)}{2} * h$

$FOV_{trapezoid} = \frac{(253.8272+65.43548)}{2} * 201.6811$

$FOV_{trapezoid} = 32194\ cm^2$

$FOV_{trapezoid}$ = 3.2194 m²

FOV_{circle}+$FOV_{trapezoid}$= 14.43 m²

Since the pan angles are based on the position at the center of the field of view, we need to add the area to the right and left of the start and end positions, respectively (i.e., one still frame, oblique field of view). This is calculated as the area of a trapezoid, where the width of the top and bottom are determined by doubling the tangent of one half the horizontal acceptance angle multiplied by the ratio of the camera height to the cosine of the angle incident with the camera lens at the top and bottom of the visible field of view (defined by the vertical acceptance angles). The trapezoid area is then added to the circle area, to reach the full area visible in the field of view in 2014.

2018 field of view

2018 Field of view

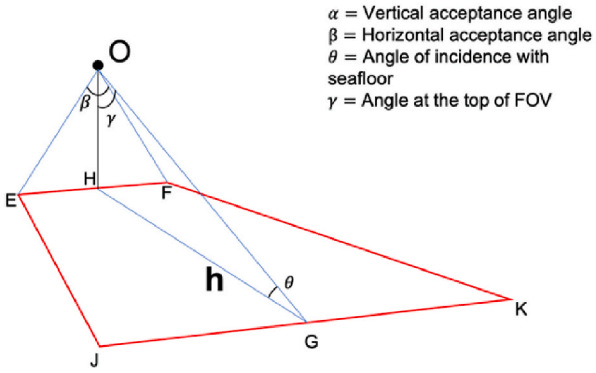

$\beta = 53.3^{\circ}$
$\gamma = 76^{\circ}$
OH = 95 cm

$JK = 2 * \tan\left(\frac{\beta}{2}\right) * \left(\frac{OH}{\cos(\gamma)}\right)$
$EF = 2 * \tan\left(\frac{\beta}{2}\right) * OH$
$h = OH * \tan(\gamma)$

$FOV_{trapezoid} = \frac{(JK+EF)}{2} * h$

$FOV_{trapezoid} = \frac{(394.1453+95.35239)}{2} * 381.0242$

$FOV_{trapezoid} = 93255.24 cm^2$

$FOV_{trapezoid}$ = 9.33 m²

In 2018, the camera starts pointing straight down, tilts up to 90°, and then tilts back to straight down. Here, we chose the angle at the top of the field of view to be 76° (angle at the center of the field of view, marked by the lasers) as this provided adequate lighting to see and count *Strongylocentrotus fragilis* but serves as a cut off to define a standardized field of view. The field of view area is calculated as the area of a trapezoid, where the width of the top and bottom are determined by doubling the tangent of one half the horizontal acceptance angle multiplied by the ratio of the camera height to the cosine of the angle incident with the camera lens at the top of the visible field of view (defined by the chosen stopping angle of 76°). The trapezoid area is the full visible field of view used to count *S. fragilis* in 2018

2019-2020 field of view

2019-2020 Field of view

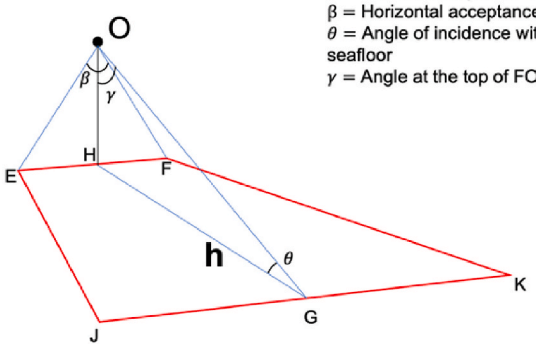

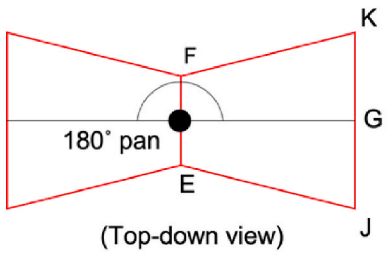

$\beta = 53.3^{\circ}$
$\gamma = 76^{\circ}$
OH = 85 cm

$JK = 2 * \tan\left(\frac{\beta}{2}\right) * \left(\frac{OH}{\cos(\gamma)}\right)$
$EF = 2 * \tan\left(\frac{\beta}{2}\right) * OH$
$h = OH * \tan(\gamma)$

$FOV_{trapezoid} = \frac{(JK+EF)}{2} * h$

$FOV_{trapezoid} = \frac{(352.6564+85.31529)}{2} * 340.9164$

$FOV_{trapezoid} = 74655.85 cm^2$

$FOV_{trapezoid}$ * 2 = 14.93 m²

In 2019-2020, the camera starts pointing straight down, tilts up to 90°, and then tilts back to straight down. Here, we chose the angle at the top of the field of view to be 76° (angle at the center of the field of view, marked by the lasers) as this provided adequate lighting to see and count

Strongylocentrotus fragilis but serves as a cut off to define a standardized field of view. The field of view area is calculated as the area of a trapezoid, where the width of the top and bottom are determined by doubling the tangent of one half the horizontal acceptance angle multiplied by the ratio of the camera height to the cosine of the angle incident with the camera lens at the top of the visible field of view (defined by the chosen stopping angle of 76°). As the 180° occurs when the camera is pointing 90°, there is no visible seafloor area during the pan. When the camera pan finishes, the visible seafloor represents a new visible area and was assumed to be equal to the first area. Thus, the trapezoid area was doubled to account for both sides of the observatory visible in 2019-2020. This doubled area was used to count *S. fragilis* in 2019-2020.

Appendix 2. Generalized additive modeling details

GAMs are an extension of generalized linear models that allow for non-linear trends to be modeled using smooth functions fj of covariates xj (hereafter "smoothers", Wood 2011). In general, these models take the form:

$$E(Y) = g^{-1}\left(\beta_0 + \sum_{j=1}^{J} f_j(x_j)\right), \quad \text{Eq. 1}$$

Where E(Y) is the expected value of the response, g-1 is the inverse-link function for the distribution of Y, and β0 is an intercept term. Smooths are represented as the sum of K basis functions (bj,k), multiplied by some coefficients (βj,k),

$$f_j(x_j) = \sum_{i=1}^{K} \beta_{j,k} b_{j,k}(x_j) \quad \text{Eq. 2}$$

In practice, K represents the upper limit on the complexity of the smoother (Wood 2011). When estimating the coefficients of each smoother, a "wiggliness penalty " needs to be applied to prevent the model overfitting the data (Wood 2011). The mgcv package (Wood 2011) in R (R Core Team 2020) enables automatic estimation of smoothness parameters using a variety of algorithms (Wood et al. 2016).

Model selection

For urchin density models, we first fit 5 temporal models: A global smoother for ST (model G), year-level smoothers for ST (model I and model S), and a global smoother with year-level smoothers for ST (model GS and model GI) following Pedersen et al. (2019). Model G includes only a global smoother, which fits a single shared smooth for ST for all years. Models I and GI allowed the shape and wiggliness penalty of the ST smooth to vary between years using by = Year, whereas models S and GS assumed all years had the same wiggliness but varied in shape using the factor smooth basis via bs = "fs" (Pedersen et al. 2019). We set the number of basis functions at k = 5 for global ST smooth and k = 12 for year-level ST smooths to avoid fitting smoothers that were too wiggly, and to determine the relative importance of global versus between-year temporal variation (Pedersen et al. 2019).

We used the select = TRUE argument when fitting models with both global and year-level smooths (Pedersen et al. 2019). This helps to perform variable selection by adding an extra penalty to each smoother, allowing mgcv to penalize model terms to a zero effect (Marra and Wood 2011). We fit each smooth using the thin-plate-regression-spline (TPRS) basis (Wood 2003), since they are the default for mgcv and perform well with fixed k (Pedersen et al. 2019). Models were selected based on AIC (Burnham et al. 2002), where the model with the lowest AIC was considered to be the best.

References

Aguzzi, J., Company, J.B., 2010. Chronobiology of deep-water decapod Crustaceans on continental margins. In: Advances in Marine Biology. Elsevier, pp. 155–225. https://doi.org/10.1016/B978-0-12-381015-1.00003-4.

Allen, S.E., de Madron, X.D., 2009. A review of the role of submarine canyons in deep-ocean exchange with the shelf. Ocean Sci. 14.

Allen, S.E., Vindeirinho, R.E., Thomson, R.E., Foreman, M.G.G., Mackas, D.L., 2001. Physical and biological processes over a submarine canyon during an upwelling event. Can. J. Fish. Aquat. Sci. 58 (4), 671–684.

Anderson, S.C., Keppel, E.A., Edwards, A.M., 2019. A reproducible data synopsis for over 100 species of British Columbia groundfish. DFO Can. Sci. Advis. Sec. Res. Doc. Available from: https://www.dfo-mpo.gc.ca/csas-sccs/Publications/ResDocs-DocRech/2019/2019_041-eng.pdf. (Accessed 5 May 2021) accessed.

Arntz, W.E., Gallardo, V.A., Gutiérrez, D., Isla, E., Levin, L.A., Mendo, J., Neira, C., Rowe, G.T., Tarazona, J., Wolff, M., 2006. El Niño and similar perturbation effects on the benthos of the Humboldt, California, and Benguela Current upwelling ecosystems. Adv. Geosci. 6, 243–265. https://doi.org/10.5194/adgeo-6-243-2006.

Asnaghi, V., Chindris, A., Leggieri, F., Scolamacchia, M., Brundu, G., Guala, I., Loi, B., Chiantore, M., Farina, S., 2020. Decreased pH impairs sea urchin resistance to predatory fish: a combined laboratory-field study to understand the fate of top-down processes in future oceans. Mar. Environ. Res. 162, 105194 https://doi.org/10.1016/j.marenvres.2020.105194.

Auth, T.D., Daly, E.A., Brodeur, R.D., Fisher, J.L., 2018. Phenological and distributional shifts in ichthyoplankton associated with recent warming in the northeast Pacific Ocean. Global Change Biol. 24 (1), 259–272. https://doi.org/10.1111/gcb.13872.

Baker, E.T., Hickey, B.M., 1986. Contemporary sedimentation processes in and around an active West Coast submarine canyon. Mar. Geol. 71 (1–2), 15–34. https://doi.org/10.1016/0025-3227(86)90031-9.

Barth, J., Fram, J., Dever, E., Risien, C., Wingard, C., Collier, R., Kearney, T., 2018. Warm blobs, low-oxygen events, and an eclipse: the ocean observatories initiative endurance array captures them all. Oceanography 31 (1), 90–97. https://doi.org/10.5670/oceanog.2018.114.

Bates, A.E., Lee, R.W., Tunnicliffe, V., Lamare, M.D., 2010. Deep-sea hydrothermal vent animals seek cool fluids in a highly variable thermal environment. Nat. Commun. 1 (1), 14. https://doi.org/10.1038/ncomms1014.

Batten, S.D., Raitsos, D.E., Danielson, S., Hopcroft, R., Coyle, K., McQuatters-Gollop, A., 2018. Interannual variability in lower trophic levels on the Alaskan Shelf. Deep Sea Res. Part II Top. Stud. Oceanogr. 147, 58–68. https://doi.org/10.1016/j.dsr2.2017.04.023.

Beaulieu, S.E., 2003. Resuspension of phytodetritus from the sea floor: a laboratory flume study. Limnol. Oceanogr. 48 (3), 1235–1244. https://doi.org/10.4319/lo.2003.48.3.1235.

Best, M.M.R., Bornhold, B.D., Juniper, S.K., Barnes, C.R., 2007. NEPTUNE Canada regional cabled observatory: science plan. In: OCEANS 2007. IEEE, Vancouver, BC, pp. 1–7. https://doi.org/10.1109/OCEANS.2007.4449316.

Bett, B.J., Malzone, M.G., Narayanaswamy, B.E., Wigham, B.D., 2001. Temporal variability in phytodetritus and megabenthic activity at the seabed in the deep Northeast Atlantic. Prog. Oceanogr. 50 (1–4), 349–368. https://doi.org/10.1016/S0079-6611(01)00066-0.

Billett, D.S.M., Bett, B.J., Reid, W.D.K., Boorman, B., Priede, I.G., 2010. Long-term Change in the Abyssal NE Atlantic the 'Amperima Event Revisited, p. 12.

Billett, D.S.M., Lampitt, R.S., Rice, A.L., Mantoura, R.F.C., 1983. Seasonal sedimentation of phytoplankton to the deep-sea benthos. Nature 302 (5908), 520–522. https://doi.org/10.1038/302520a0.

Birchenough, S.N.R., Reiss, H., Degraer, S., Mieszkowska, N., Borja, Á., Buhl-Mortensen, L., Braeckman, U., Craeymeersch, J., De Mesel, I., Kerckhof, F., Kröncke, I., Parra, S., Rabaut, M., Schröder, A., Van Colen, C., Van Hoey, G., Vincx, M., Wätjen, K., 2015. Climate change and marine benthos: a review of existing research and future directions in the North Atlantic. WIREs Clim. Change 6 (2), 203–223. https://doi.org/10.1002/wcc.330.

Bond, N.A., Cronin, M.F., Freeland, H., Mantua, N., 2015. Causes and impacts of the 2014 warm anomaly in the NE Pacific: Geophys. Res. Lett. 42 (9), 3414–3420. https://doi.org/10.1002/2015GL063306.

Booloottian, R.A., Giese, A.C., Tucker, J.S., Farmanfarmaian, A., 1959. A contribution to the biology of a deep sea echinoid, Allocentrotus fragilis (Jackson). Biol. Bull. 116 (3), 362–372. https://doi.org/10.2307/1538946.
Brodeur, R.D., Auth, T.D., Phillips, A.J., 2019. Major shifts in pelagic micronekton and macrozooplankton community structure in an upwelling ecosystem related to an unprecedented marine heatwave. Front. Mar. Sci. 6, 212. https://doi.org/10.3389/fmars.2019.00212.
Buja, A., Hastie, T., Tibshirani, R., 1989. Linear smoothers and additive models. Ann. Stat. 17 (2), 453–555.
Burnham, K.P., Anderson, D.R., Burnham, K.P., 2002. Model Selection and Multimodel Inference: a Practical Information-Theoretic Approach, second ed. Springer, New York.
Campanyà-Llovet, N., Snelgrove, P.V.R., De Leo, F.C., 2018. Food quantity and quality in Barkley Canyon (NE Pacific) and its influence on macroinfaunal community structure. Prog. Oceanogr. 169, 106–119. https://doi.org/10.1016/j.pocean.2018.04.003.
Cavole, L.M., Demko, A., Diner, R., Giddings, A., Koester, I., Pagniello, C., Paulsen, M.-L., Ramirez-Valdez, A., Schwenck, S., Yen, N., Zill, M., Franks, P., 2016. Biological impacts of the 2013–2015 warm-water anomaly in the Northeast Pacific: winners, losers, and the future. Oceanography 29 (2). https://doi.org/10.5670/oceanog.2016.32.
Chanson, H., Takeuchi, M., Trevethan, M., 2008. Using turbidity and acoustic backscatter intensity as surrogate measures of suspended sediment concentration in a small subtropical estuary. J. Environ. Manag. 88 (4), 1406–1416. https://doi.org/10.1016/j.jenvman.2007.07.009.
Chatzievangelou, D., Aguzzi, J., Ogston, A., Suárez, A., Thomsen, L., 2020. Visual monitoring of key deep-sea megafauna with an Internet Operated crawler as a tool for ecological status assessment. Prog. Oceanogr. 184, 102321 https://doi.org/10.1016/j.pocean.2020.102321.
Chatzievangelou, D., Doya, C., Thomsen, L., Purser, A., Aguzzi, J., 2016. High-frequency patterns in the abundance of benthic species near a cold-seep – an internet operated vehicle application. PLoS One 11 (10), e0163808. https://doi.org/10.1371/journal.pone.0163808.
Chauvet, P., 2018. Etude de la dynamique temporelle et environnementale contrôlant la mégafaune profonde vivant dans le Canyon de Barkley grâce à l'utilisation de l'observatoire Ocean Network Canada. PhD, Université de Bretagne occidentale (Brest).
Chauvet, P., Metaxas, A., Hay, A.E., Matabos, M., 2018. Annual and seasonal dynamics of deep-sea megafaunal epibenthic communities in Barkley Canyon (British Columbia, Canada): a response to climatology, surface productivity and benthic boundary layer variation. Prog. Oceanogr. 169, 89–105. https://doi.org/10.1016/j.pocean.2018.04.002.
Chauvet, P., Metaxas, A., Matabos, M., 2019. Interannual variation in the population dynamics of juveniles of the deep-sea crab Chionoecetes tanneri. Front. Mar. Sci. 6, 50. https://doi.org/10.3389/fmars.2019.00050.
Chavez, F.P., Messié, M., 2009. A comparison of eastern boundary upwelling ecosystems. Prog. Oceanogr. 83 (1–4), 80–96. https://doi.org/10.1016/j.pocean.2009.07.032.
Conover, W.J., 1971. Practical Nonparametric Statistics. John Wiley & Sons, Ltd, New York.
Couch, C.S., Burns, J.H.R., Liu, G., Steward, K., Gutlay, T.N., Kenyon, J., Eakin, C.M., Kosaki, R.K., 2017. Mass coral bleaching due to unprecedented marine heatwave in papahānaumokuākea marine national monument (northwestern Hawaiian islands). PLoS One 12 (9), e0185121. https://doi.org/10.1371/journal.pone.0185121.
De Leo, F.C., Gauthier, M., Nephin, J., Mihály, S., Juniper, S.K., 2017. Bottom trawling and oxygen minimum zone influences on continental slope benthic community structure off Vancouver Island (NE Pacific). Deep Sea Res. Part II Top. Stud. Oceanogr. 137, 404–419. https://doi.org/10.1016/j.dsr2.2016.11.014.
De Leo, F.C., Ogata, B., Sastri, A.R., Heesemann, M., Mihály, S., Galbraith, M., Morley, M. G., 2018. High-frequency observations from a deep-sea cabled observatory reveal seasonal overwintering of Neocalanus spp. in Barkley Canyon, NE Pacific: insights into particulate organic carbon flux. Prog. Oceanogr. 169, 120–137. https://doi.org/10.1016/j.pocean.2018.06.001.
Delorme, N.J., Sewell, M.A., 2014. Temperature and salinity: two climate change stressors affecting early development of the New Zealand sea urchin Evechinus chloroticus. Mar. Biol. 161 (9), 1999–2009. https://doi.org/10.1007/s00227-014-2480-0.
Domke, L., Lacharité, M., Metaxas, A., Matabos, M., 2017. Influence of an oxygen minimum zone and macroalgal enrichment on benthic megafaunal community composition in a NE Pacific submarine canyon. Mar. Ecol. 38 (6), e12481 https://doi.org/10.1111/maec.12481.
Doya, C., Aguzzi, J., Pardo, M., Matabos, M., Company, J.B., Costa, C., Mihaly, S., Canals, M., 2014. Diel behavioral rhythms in sablefish (Anoplopoma fimbria) and other benthic species, as recorded by the Deep-sea cabled observatories in Barkley canyon (NEPTUNE-Canada). J. Mar. Syst. 130, 69–78. https://doi.org/10.1016/j.jmarsys.2013.04.003.
Drazen, J.C., Baldwin, R.J., Smith, K.L., 1998. Sediment community response to a temporally varying food supply at an abyssal station in the NE pacific. Deep Sea Res. Part II Top. Stud. Oceanogr. 45 (4–5), 893–913. https://doi.org/10.1016/S0967-0645(98)00007-1.
Dunn, O.J., 1964. Multiple comparisons using rank sums. Technometrics 6 (3), 241–252. https://doi.org/10.1080/00401706.1964.10490181.
Durden, J.M., Bett, B.J., Huffard, C.L., Pebody, C., Ruhl, H.A., Smith, K.L., 2020. Response of deep-sea deposit-feeders to detrital inputs: a comparison of two abyssal time-series sites. Deep Sea Res. Part II Top. Stud. Oceanogr. 173, 104677 https://doi.org/10.1016/j.dsr2.2019.104677.
Dwinovantyo, A., Manik, H.M., Prartono, T., Susilohadi, Ilahude, D., 2017. Estimation of suspended sediment concentration from acoustic Doppler current profiler (ADCP) instrument: a case study of Lembeh strait, North Sulawesi. IOP Conf. Ser. Earth Environ. Sci. 54, 012082 https://doi.org/10.1088/1755-1315/54/1/012082.
Edwards, M.S., 2004. Estimating scale-dependency in disturbance impacts: el Niños and giant kelp forests in the northeast Pacific. Oecologica 138, 436–447. https://doi.org/10.1007/s00442-003-1452-8.
Filbee-Dexter, K., Scheibling, R., 2014. Detrital kelp subsidy supports high reproductive condition of deep-living sea urchins in a sedimentary basin. Aquat. Biol. 23 (1), 71–86. https://doi.org/10.3354/ab00607.
Fredriksen, R., Christiansen, J.S., Bonsdorff, E., Larsen, L.-H., Nordström, M.C., Zhulay, I., Bluhm, B.A., 2020. Epibenthic megafauna communities in Northeast Greenland vary across coastal, continental shelf and slope habitats. Polar Biol. 43 (10), 1623–1642. https://doi.org/10.1007/s00300-020-02733-z.
Gage, J.D., Tyler, P.A., 1991. Deep-Sea Biology: A Natural History of Organisms at the Deep-Sea Floor. Cambridge University Press, Cambridge.
Genin, A., 2004. Bio-physical coupling in the formation of zooplankton and fish aggregations over abrupt topographies. J. Mar. Syst. 50 (1–2), 3–20. https://doi.org/10.1016/j.jmarsys.2003.10.008.
Gleason, L.U., Burton, R.S., 2013. Phenotypic evidence for local adaptation to heat stress in the marine snail Chlorostoma (formerly Tegula) funebralis. J. Exp. Mar. Biol. Ecol. 448, 360–366. https://doi.org/10.1016/j.jembe.2013.08.008.
Glover, A.G., Gooday, A.J., Bailey, D.M., Billett, D.S.M., Chevaldonné, P., Colaço, A., Copley, J., Cuvelier, D., Desbruyères, D., Kalogeropoulou, V., Klages, M., Lampadariou, N., Lejeusne, C., Mestre, N.C., Paterson, G.L.J., Perez, T., Ruhl, H., Sarrazin, J., Soltwedel, T., Soto, E.H., Thatje, S., Tselepides, A., Van Gaever, S., Vanreusel, A., 2010. Temporal change in deep-sea benthic ecosystems. In: Advances in Marine Biology. Elsevier, pp. 1–95. https://doi.org/10.1016/B978-0-12-381015-1.00001-0.
Haalboom, S., de Stigter, H., Duineveld, G., van Haren, H., Reichart, G.-J., Mienis, F., 2021. Suspended particulate matter in a submarine canyon (Whittard Canyon, Bay of Biscay, NE Atlantic Ocean): assessment of commonly used instruments to record turbidity. Mar. Geol. 434, 106439 https://doi.org/10.1016/j.margeo.2021.106439.
Harrold, C., Light, K., Lisin, S., 1998. Organic enrichment of submarine-canyon and continental-shelf benthic communities by macroalgal drift imported from nearshore kelp forests. Limnol. Oceanogr. 43 (4), 669–678. https://doi.org/10.4319/lo.1998.43.4.0669.
Hayes, N.M., Haig, H.A., Simpson, G.L., Leavitt, P.R., 2020. Effects of lake warming on the seasonal risk of toxic cyanobacteria exposure. Limnol. Oceanogr. 5 (6), 393–402. https://doi.org/10.1002/lol2.10164.
Heise, K., 2006. Oxidative stress during stressful heat exposure and recovery in the North Sea eelpout Zoarces viviparus L. J. Exp. Biol. 209 (2), 353–363. https://doi.org/10.1242/jeb.01977.
Helly, J.J., Levin, L.A., 2004. Global distribution of naturally occurring marine hypoxia on continental margins. Deep Sea Res. Oceanogr. Res. Pap. 51 (9), 1159–1168. https://doi.org/10.1016/j.dsr.2004.03.009.
Hickey, B.M., 1979. The California current system—hypotheses and facts. Prog. Oceanogr. 8 (4), 191–279. https://doi.org/10.1016/0079-6611(79)90002-8.
Hoitink, A.J.F., Hoekstra, P., 2005. Observations of suspended sediment from ADCP and OBS measurements in a mud-dominated environment. Coast Eng. 52 (2), 103–118. https://doi.org/10.1016/j.coastaleng.2004.09.005.
Honjo, S., Eglinton, T., Taylor, C., Ulmer, K., Sievert, S., Bracher, A., German, C., Edgcomb, V., Francois, R., Iglesias-Rodriguez, M.D., Van Mooy, B., Rapeta, D., 2014. Understanding the role of the biological pump in the global carbon cycle: an imperative for ocean science. oceanog 27 (3), 10–16. https://doi.org/10.5670/oceanog.2014.78.
Jackson, J.M., Johnson, G.C., Dosser, H.V., Ross, T., 2018a. Warming from recent marine heatwave lingers in deep British Columbia fjord. Geophys. Res. Lett. 45 (18), 9757–9764. https://doi.org/10.1029/2018GL078971.
Jackson, R., Gabric, A., Cropp, R., 2018b. Effects of ocean warming and coral bleaching on aerosol emissions in the Great Barrier Reef, Australia. Sci. Rep. 8 (1), 14048 https://doi.org/10.1038/s41598-018-32470-7.
Juniper, S.K., Matabos, M., Mihály, S., Ajayamohan, R.S., Gervais, F., Bui, A.O.V., 2013. A year in Barkley Canyon: a time-series observatory study of mid-slope benthos and habitat dynamics using the NEPTUNE Canada network. Deep Sea Res. Part II Top. Stud. Oceanogr. 92, 114–123. https://doi.org/10.1016/j.dsr2.2013.03.038.
Kelly, M.W., Pankey, M.S., DeBiasse, M.B., Plachetzki, D.C., 2017. Adaptation to heat stress reduces phenotypic and transcriptional plasticity in a marine copepod. Funct. Ecol. 31 (2), 398–406. https://doi.org/10.1111/1365-2435.12725.
Kendzierska, H., Łukawska-Matuszewska, K., Burska, D., Janas, U., 2020. Benthic fluxes of oxygen and nutrients under the influence of macrobenthic fauna on the periphery of the intermittently hypoxic zone in the Baltic Sea. J. Exp. Mar. Biol. Ecol. 530–531. https://doi.org/10.1016/j.jembe.2020.151439, 151439.
Kintisch, E., 2015. 'The Blob' invades Pacific, flummoxing climate experts. Science 348 (6230), 17–18. https://doi.org/10.1126/science.348.6230.17.
Kruskal, W.H., Wallis, W.A., 1952. Use of ranks in one-criterion variance analysis. J. Am. Stat. Assoc. 47 (260), 583–621. https://doi.org/10.1080/01621459.1952.10483441.
Kuhnz, L.A., Ruhl, H.A., Huffard, C.L., Smith, K.L., 2020. Benthic megafauna assemblage change over three decades in the abyss: variations from species to functional groups. Deep Sea Res. Part II Top. Stud. Oceanogr. 173, 104761 https://doi.org/10.1016/j.dsr2.2020.104761.
Lampitt, R.S., 1985. Evidence for the seasonal deposition of detritus to the deep-sea floor and its subsequent resuspension. Deep Sea Research Part A. Oceanogr. Res. Pap. 32 (8), 885–897. https://doi.org/10.1016/0198-0149(85)90034-2.

Lara-Lopez, A., Neira, F.J., 2008. Synchronicity between zooplankton biomass and larval fish concentrations along a highly flushed Tasmanian estuary: assessment using net and acoustic methods. J. Plankton Res. 30 (9), 1061–1073. https://doi.org/10.1093/plankt/fbn063.

Lebrato, M., Iglesias-Rodríguez, D., Feely, R.A., Greeley, D., Jones, D.O.B., Suarez-Bosche, N., Lampitt, R.S., Cartes, J.E., Green, D.R.H., Alker, B., 2010. Global contribution of echinoderms to the marine carbon cycle: CaCO $_3$ budget and benthic compartments. Ecol. Monogr. 80 (3), 441–467. https://doi.org/10.1890/09-0553.1.

Leising, A.W., Schroeder, I.D., Bograd, S.J., Abell, J., Durazo, R., Gaxiola-Castro, G., Marinas, U.-F. de C., Playitas, Z., 2015. State of the California Current 2014–15: Impacts of the Warm-Water "Blob, vol. 56, p. 38.

Levin, L.A., 2003. Oxygen minimum zone benthos: adaptation and community response to hypoxia. Oceanogr. Mar. Biol. Annu. Rev. 41, 1–45.

Levin, L.A., Liu, K.-K., Emeis, K.-C., Breitburg, D.L., Cloern, J., Deutsch, C., Giani, M., Goffart, A., Hofmann, E.E., Lachkar, Z., Limburg, K., Liu, S.-M., Montes, E., Naqvi, W., Ragueneau, O., Rabouille, C., Sarkar, S.K., Swaney, D.P., Wassman, P., Wishner, K.F., 2015. Comparative biogeochemistry–ecosystem–human interactions on dynamic continental margins. J. Mar. Syst. 141, 3–17. https://doi.org/10.1016/j.jmarsys.2014.04.016.

Levin, L.A., Sibuet, M., 2012. Understanding continental margin biodiversity: a new imperative. Ann. Rev. Mar. Sci 4 (1), 79–112. https://doi.org/10.1146/annurev-marine-120709-142714.

Lin, X., Zhang, D., 1999. Inference in generalized additive mixed modelsby using smoothing splines. J. Roy. Stat. Soc. B 61 (2), 381–400. https://doi.org/10.1111/1467-9868.00183.

Low, N.H.N., Micheli, F., 2020. Short- and long-term impacts of variable hypoxia exposures on kelp forest sea urchins. Sci. Rep. 10 (1), 2632. https://doi.org/10.1038/s41598-020-59483-5.

Mackas, D.L., Kieser, R., Saunders, M., Yelland, D.R., Brown, R.M., Moore, D.F., 1997. Aggregation of euphausiids and Pacific hake (Merluccius productus) along the outer continental shelf off Vancouver Island. Can. J. Fish. Aquat. Sci. 54 (9), 2080–2096. https://doi.org/10.1139/f97-113.

Matabos, M., Bui, A.O.V., Mihály, S., Aguzzi, J., Juniper, S.K., Ajayamohan, R.S., 2014. High-frequency study of epibenthic megafaunal community dynamics in Barkley Canyon: a multi-disciplinary approach using the NEPTUNE Canada network. J. Mar. Syst. 130, 56–68. https://doi.org/10.1016/j.jmarsys.2013.05.002.

McBride, S.C., Pinnix, W.D., Lawrence, J.M., Lawrence, A.L., Mulligan, T.M., 1997. The effect of temperature on production of gonads by the sea urchin Strongylocentrotus franciscanus fed natural and prepared diets. J. World Aquacult. Soc. 28 (4), 357–365. https://doi.org/10.1111/j.1749-7345.1997.tb00282.x.

McCabe, R.M., Hickey, B.M., Kudela, R.M., Lefebvre, K.A., Adams, N.G., Bill, B.D., Gulland, F.M.D., Thomson, R.E., Cochlan, W.P., Trainer, V.L., 2016. An unprecedented coastwide toxic algal bloom linked to anomalous ocean conditions. Geophys. Res. Lett. 43 (19) https://doi.org/10.1002/2016GL070023.

McGowan, J.A., 1998. Climate-Ocean variability and ecosystem response in the Northeast Pacific. Science 281 (5374), 210–217. https://doi.org/10.1126/science.281.5374.210.

McKibben, S.M., Peterson, W., Wood, A.M., Trainer, V.L., Hunter, M., White, A.E., 2017. Climatic regulation of the neurotoxin domoic acid. Proc. Natl. Acad. Sci. U.S.A. 114 (2), 239–244. https://doi.org/10.1073/pnas.1606798114.

McPherson, M.L., Finger, D.J.I., Houskeeper, H.F., Bell, T.W., Carr, M.H., Rogers-Bennett, L., Kudela, R.M., 2021. Large-scale shift in the structure of a kelp forest ecosystem co-occurs with an epizootic and marine heatwave. Commun. Biol. 4 (298) https://doi.org/10.1038/s42003-021-01827-6.

Morford, J.L., Emerson, S., 1999. The geochemistry of redox sensitive trace metals in sediments. Geochem. Cosmochim. Acta 63 (11/12), 1735–1750.

Morlini, I., 2006. On multicollinearity and concurvity in some nonlinear multivariate models. JISS 15 (1), 3–26. https://doi.org/10.1007/s10260-006-0005-9.

Nakajima, R., Komuku, T., Yamakita, T., Lindsay, D.J., Jintsu-Uchifune, Y., Watanabe, H., Tanaka, K., Shirayama, Y., Yamamoto, H., Fujikura, K., 2014. A new method for estimating the area of the seafloor from oblique images taken by deep-sea submersible survey platforms. JAMSTEC-R 19, 59–66. https://doi.org/10.5918/jamstecr.19.59, 0.

Oliver, E.C.J., Donat, M.G., Burrows, M.T., Moore, P.J., Smale, D.A., Alexander, L.V., Benthuysen, J.A., Feng, M., Sen Gupta, A., Hobday, A.J., Holbrook, N.J., Perkins-Kirkpatrick, S.E., Scannell, H.A., Straub, S.C., Wernberg, T., 2018. Longer and more frequent marine heatwaves over the past century. Nat. Commun. 9 (1), 1324. https://doi.org/10.1038/s41467-018-03732-9.

Papiol, V., Hendrickx, M.E., Serrano, D., 2017. Effects of latitudinal changes in the oxygen minimum zone of the northeast Pacific on the distribution of bathyal benthic decapod crustaceans. Deep Sea Res. Part II Top. Stud. Oceanogr. 137, 113–130. https://doi.org/10.1016/j.dsr2.2016.04.023.

Pierce, S.D., Barth, J.A., Shearman, R.K., Erofeev, A.Y., 2012. Declining oxygen in the Northeast Pacific. J. Phys. Oceanogr. 42 (3), 495–501. https://doi.org/10.1175/JPO-D-11-0170.1.

Pohlert, T., 2021. PMCMRplus: calculate pairwise multiple comparisons of mean rank sums extended. Available from: https://CRAN.R-project.org/package=PMCMRplus.

Puig, P., Palanques, A., Martín, J., 2014. Contemporary sediment-transport processes in submarine canyons. Ann. Rev. Mar. Sci 6 (1), 53–77. https://doi.org/10.1146/annurev-marine-010213-135037.

R Core Team, 2020. R: A Language and Environment for Statistical Computing. R Foundation for Statistical Computing, Vienna, Austria. Available from: https://www.Rproject.org/.

Ramos-Musalem, K., Allen, S.E., 2019. The impact of locally enhanced vertical diffusivity on the cross-shelf transport of tracers induced by a submarine canyon. J. Phys. Oceanogr. 49, 24.

Ritzman, J., Brodbeck, A., Brostrom, S., McGrew, S., Dreyer, S., Klinger, T., Moore, S.K., 2018. Economic and sociocultural impacts of fisheries closures in two fishing-dependent communities following the massive 2015 U.S. West Coast harmful algal bloom. Harmful Algae 80, 35–45. https://doi.org/10.1016/j.hal.2018.09.002.

Robert, K., Juniper, S., 2012. Surface-sediment bioturbation quantified with cameras on the NEPTUNE Canada cabled observatory. Mar. Ecol. Prog. Ser. 453, 137–149. https://doi.org/10.3354/meps09623.

Ross, T., Du Preez, C., Ianson, D., 2020. Rapid deep ocean deoxygenation and acidification threaten life on Northeast Pacific seamounts. Global Change Biol.: gcb.15307 https://doi.org/10.1111/gcb.15307.

Rossi, V., López, C., Hernández-García, E., Sudre, J., Garçon, V., Morel, Y., 2009. Surface mixing and biological activity in the four eastern boundary upwelling systems. Nonlinear Process Geophys. 16 (4), 557–568. https://doi.org/10.5194/npg-16-557-2009.

Ruhl, H.A., Smith, Kenneth L., 2004. Shifts in deep-sea community structure linked to climate and food supply. Science 305 (5683), 513–515. https://doi.org/10.1126/science.1099759.

Sato, K.N., Andersson, A.J., Day, J.M.D., Taylor, J.R.A., Frank, M.B., Jung, J.-Y., McKittrick, J., Levin, L.A., 2018. Response of sea urchin fitness traits to environmental gradients across the southern California oxygen minimum zone. Front. Mar. Sci. 5, 258. https://doi.org/10.3389/fmars.2018.00258.

Sato, K.N., Levin, L.A., Schiff, K., 2017. Habitat compression and expansion of sea urchins in response to changing climate conditions on the California continental shelf and slope (1994–2013). Deep Sea Res. Part II Top. Stud. Oceanogr. 137, 377–389. https://doi.org/10.1016/j.dsr2.2016.08.012.

Scannell, H.A., Pershing, A.J., Alexander, M.A., Thomas, A.C., Mills, K.E., 2016. Frequency of marine heatwaves in the North Atlantic and north pacific since 1950: frequency of marine heatwaves since 1950. Geophys. Res. Lett. 43 (5), 2069–2076. https://doi.org/10.1002/2015GL067308.

Shapiro, S.S., Wilk, M.B., 1965. An analysis of variance test for normality (complete samples). Biometrika 52 (3), 591–611. https://doi.org/10.1093/biomet/52.3-4.591.

Smith Jr., K.L., 1999. Long-term discrepancy between food supply and demand in the deep eastern north pacific. Science 284 (5417), 1174–1177. https://doi.org/10.1126/science.284.5417.1174.

Smith, K.L., Kaufmann, R.S., Baldwin, R.J., 1994. Coupling of near-bottom pelagic and benthic processes at abyssal depths in the eastern North Pacific Ocean. Limnol. Oceanogr. 39 (5), 1101–1118. https://doi.org/10.4319/lo.1994.39.5.1101.

Smith, K.L., Kaufmann, R.S., Wakefield, W.W., 1993. Mobile megafaunal activity monitored with a time-lapse camera in the abyssal North Pacific. Deep Sea Res. Oceanogr. Res. Pap. 40 (11–12), 2307–2324. https://doi.org/10.1016/0967-0637(93)90106-D.

Smith, K.L., Ruhl, H.A., Huffard, C.L., Messié, M., Kahru, M., 2018. Episodic organic carbon fluxes from surface ocean to abyssal depths during long-term monitoring in NE Pacific. Proc. Natl. Acad. Sci. U.S.A. 115 (48), 12235–12240. https://doi.org/10.1073/pnas.1814559115.

Sorte, C.J.B., Fuller, A., Bracken, M.E.S., 2010. Impacts of a simulated heat wave on composition of a marine community. Oikos 119 (12), 1909–1918. https://doi.org/10.1111/j.1600-0706.2010.18663.x.

Starko, S., Bailey, L.A., Creviston, E., James, K.A., Warren, A., Brophy, M.K., Danasel, A., Fass, M.P., Townsend, J.A., Neufeld, C.J., 2019. Environmental heterogeneity mediates scale-dependent declines in kelp diversity on intertidal rocky shores. PLoS One 14 (3), e0213191. https://doi.org/10.1371/journal.pone.0213191.

Sumich, J.L., McCauley, J.E., 1973. Growth of a Sea urchin, allocentrotus fragilis, off the Oregon coast. Pac. Sci. 27 (2), 156–167.

Suryan, R.M., Arimitsu, M.L., Coletti, H.A., Hopcroft, R.R., Lindeberg, M.R., Barbeaux, S. J., Batten, S.D., Burt, W.J., Bishop, M.A., Bodkin, J.L., Brenner, R., Campbell, R.W., Cushing, D.A., Danielson, S.L., Dorn, M.W., Drummond, B., Esler, D., Gelatt, T., Hanselman, D.H., Hatch, S.A., Haught, S., Holderied, K., Iken, K., Irons, D.B., Kettle, A.B., Kimmel, D.G., Konar, B., Kuletz, K.J., Laurel, B.J., Maniscalco, J.M., Matkin, C., McKinstry, C.A.E., Monson, D.H., Moran, J.R., Olsen, D., Palsson, W.A., Pegau, W.S., Piatt, J.F., Rogers, L.A., Rojek, N.A., Schaefer, A., Spies, I.B., Straley, J. M., Strom, S.L., Sweeney, K.L., Szymkowiak, M., Weitzman, B.P., Yasumiishi, E.M., Zador, S.G., 2021. Ecosystem response persists after a prolonged marine heatwave. Sci. Rep. 11 https://doi.org/10.1038/s41598-021-83818-5.

Taylor, J.R., Lovera, C., Whaling, P.J., Buck, K.R., Pane, E.F., Barry, J.P., 2014. Physiological effects of environmental acidification in the deep-sea urchin *Strongylocentrotus fragilis*. Biogeosciences 11 (5), 1413–1423. https://doi.org/10.5194/bg-11-1413-2014.

Thompson, B., Riddle, M., 2005. Bioturbation behaviour of the spatangoid urchin Abatus ingens in Antarctic marine sediments. Mar. Ecol. Prog. Ser. 290, 135–143. https://doi.org/10.3354/meps290135.

Thomsen, L., Aguzzi, J., Costa, C., De Leo, F., Ogston, A., Purser, A., 2017. The oceanic biological pump: rapid carbon transfer to depth at continental margins during winter. Sci. Rep. 7 (1), 10763 https://doi.org/10.1038/s41598-017-11075-6.

Trainer, V.L., Moore, S.K., Hallegraeff, G., Kudela, R.M., Clement, A., Mardones, J.I., Cochlan, W.P., 2020. Pelagic harmful algal blooms and climate change: lessons from nature's experiments with extremes. Harmful Algae 91, 101591. https://doi.org/10.1016/j.hal.2019.03.009.

Tseng, Y.-H., Ding, R., Huang, X., 2017. The warm Blob in the northeast Pacific—the bridge leading to the 2015/16 El Niño. Environ. Res. Lett. 12 (5), 054019 https://doi.org/10.1088/1748-9326/aa67c3.

Turner, J.T., 2015. Zooplankton fecal pellets, marine snow, phytodetritus and the ocean's biological pump. Prog. Oceanogr. 130, 205–248. https://doi.org/10.1016/j.pocean.2014.08.005.

Vetter, E., Dayton, P., 1999. Organic enrichment by macrophyte detritus, and abundance patterns of megafaunal populations in submarine canyons. Mar. Ecol. Prog. Ser. 186, 137–148. https://doi.org/10.3354/meps186137.

Vopel, K., Vopel, A., Thistle, D., Hancock, N., 2007. Effects of spatangoid heart urchins on O2 supply into coastal sediment. Mar. Ecol. Prog. Ser. 333, 161–171. https://doi.org/10.3354/meps333161.

Wakefield, W.W., Genin, A., 1987. The use of a Canadian (perspective) grid in deep-sea photography. Deep Sea Research Part A. Oceanogr. Res. Pap. 34 (3), 469–478. https://doi.org/10.1016/0198-0149(87)90148-8.

Ware, D.M., Thomson, R.E., 1991. Link between long-term variability in upwelling and fish production in the Northeast Pacific ocean. Can. J. Fish. Aquat. Sci. 48 (12), 2296–2306. https://doi.org/10.1139/f91-270.

Whitney, F.A., Freeland, H.J., Robert, M., 2007. Persistently declining oxygen levels in the interior waters of the eastern subarctic Pacific. Prog. Oceanogr. 75 (2), 179–199. https://doi.org/10.1016/j.pocean.2007.08.007.

Widder, E.A., Robison, B.H., Reisenbichler, K.R., Haddock, S.H.D., 2005. Using red light for in situ observations of deep-sea fishes. Deep Sea Res. Oceanogr. Res. Pap. 52 (11), 2077–2085. https://doi.org/10.1016/j.dsr.2005.06.007.

Wood, S.N., 2011. Fast stable REML and ML estimation of semiparametric GLMs. J. Roy. Stat. Soc. B 73 (1), 3–36. https://doi.org/10.1111/j.1467-9868.2010.00749.x.

Wood, S.N., Pya, N., Säfken, B., 2016. Smoothing parameter and model selection for general smooth models. J. Am. Stat. Assoc. 111 (516), 1548–1563. https://doi.org/10.1080/01621459.2016.1180986.

Yang, B., Emerson, S.R., Peña, M.A., 2018. The effect of the 2013–2016 high temperature anomaly in the subarctic Northeast Pacific (the "Blob") on net community production. Biogeosciences 15 (21), 6747–6759. https://doi.org/10.5194/bg-15-6747-2018.

Zhao, C., Liu, P., Zhou, H., Tian, X., Chang, Y., 2013. Diel observation on the distribution of the sea urchin *Strongylocentrotus intermedius* under different food availability and shelter conditions in the laboratory. Mar. Freshw. Behav. Physiol. 45 (6), 357–364. https://doi.org/10.1080/10236244.2013.763456.

Zuur, A.F., Ieno, E.N., Walker, N., Saveliev, A.A., Smith, G.M., 2009. Mixed Effects Models and Extensions in Ecology with R. Springer New York, New York, NY. https://doi.org/10.1007/978-0-387-87458-6.